

An Integrated MMW Radar System for Outdoor Navigation

Dirk Langer

January 1997

A dissertation submitted in partial fulfillment
of the requirements for the degree of
Doctor of Philosophy in Robotics

The Robotics Institute
Carnegie Mellon University
5000 Forbes Avenue
Pittsburgh, PA 15213

Copyright © 1997 Dirk Langer

This research was supported by TACOM in contract DAAE07-90-C-R059 and DAAE07-96-C-X075 ,
'CMU Autonomous Ground Vehicle' and US DOT in agreement DTFH61-94-X-00001, 'Automated Highway System'.

The views and conclusions expressed in this document are those of the author and should not be interpreted as representing the official policies, either express or implied, of the US government.

Abstract

This thesis research presents the design and evaluation of an integrated sensor system for obstacle detection and collision avoidance for automobile vehicles and mobile robot outdoor navigation. We performed evaluation tests for autonomous and manual driving modes.

At the core of the system is a 77 GHz MMW radar sensor that is able to operate robustly even under adverse weather conditions. This sensor has a range of approximately 200 metres and uses a linear array of receivers and wavefront reconstruction techniques to compute range and bearing of objects within a horizontal field of view of 12 degrees. We discuss signal processing and calibration techniques and present results obtained from simulation and the real sensor.

Clutter rejection and the ability to classify and differentiate between objects in different road lanes and off-road is improved by integration of the radar data with information from a road geometry perception system. Road geometry perception is based on either of two systems: the first one detects road lane markers or other features parallel to the road through a video camera and thereby computes vehicle position and orientation with respect to the current driving lane; the second system uses a digital road map in combination with a GPS and heading gyroscope unit to compute vehicle location and orientation on the road. Finally, we discuss the performance results obtained for both systems.

The integrated sensor system can thus operate as a copilot to a human driver for speed control with respect to traffic density and as a safety monitor for lane changing. In addition, it is able to interact with other modules, such as road followers and higher level planners, for complete autonomous driving.

An Integrated MMW Radar System for Outdoor Navigation

Acknowledgements

To my parents, Ursula and Horst Langer, who have always given me encouragement, support and guidance in pursuit of my aspirations.

The work presented in this thesis would not have been possible without the contributions of many people.

First, I would like to express my thanks to Takeo Kanade and my two advisors Martial Hebert and Chuck Thorpe for providing a marvelous research environment and stimulating discussions, not all of them research related, over many years. Also, Raj Reddy for giving me the opportunity initially to come to CMU which eventually resulted in work on this dissertation.

I thank my other committee members, Richard Stern and Roman Kuc, for their guidance and feedback throughout this research.

Michael Rozmann from the Technical University in Munich, Germany, helped me in many long discussions to learn about high frequency electronics and understand the sometimes black magic of millimeter wave radar. His suggestions and feedback were essential in the design of the radar sensor. Chris Koh and Ken Wood at Millitech corporation then built the millimeter wave front end of the radar. Thanks to Markus Mettenleiter for designing the electronics of the radar back end and to Peter Krueger for building parts of it.

For their patience and joint effort in making the integrated systems work, many thanks to Todd Jochem and Bala Kumar.

For their valuable help and advice on a variety of topics, the people who contributed are Omead Amidi, Christoph Fröhlich, Volker Gengenbach,

An Integrated MMW Radar System for Outdoor Navigation

Richard Madison, Rahul Sukthankar, Dean Pomerleau, the folks from SCS facilities, Jim Frazier and John Kozar who keep our test vehicles running, and Theona Stefanis for proofreading the entire document.

Last, but not least, I would like to thank all of my friends and colleagues in Pittsburgh, not mentioned so far, who have made living and working in this city an enjoyable experience.

This research was supported by TACOM in contract DAAE07-90-C-R059 and DAAE07-96-C-X075, 'CMU Autonomous Ground Vehicle' and US DOT in agreement DTFH61-94-X-00001, 'Automated Highway System'. Part of this work was conducted on a testbed vehicle provided by Delco Electronics.

Figure 1.4 is a still shot taken from the movie, *The Cars that Ate Paris* by Peter Weir, 1974. The picture appeared in the issue of *The Economist*, April 29th, 1995. The copyright was last owned by Hemdale, Los Angeles, as on record at the Ronald Grant Archive, London. Every effort was made to find the current copyright owner, on a trail that also lead to Crawford Productions in Australia, but no information was available. Any inquiries should therefore be directed to the author.

Figure 4.13 is copyright Etak Inc., Menlo Park, CA.

Contents

Abstract.....	i
Acknowledgements.....	iii
Contents	v
List of Figures.....	ix
1 Introduction	1
1.1 Background and Overview	2
1.2 A Brief History of Radar.....	5
1.3 Related Work.....	7
1.4 Thesis Outline	8
2 Sensor Design Concept	11
2.1 Geometry	11

2.2	Radar Specifications	13
2.2.1	<i>Antenna Design and Transmitter Power</i>	16
2.2.2	<i>Range and Angular Accuracy</i>	19
2.3	Signal Processing	21
2.3.1	<i>FMCW Radar Simulator</i>	21
2.3.2	<i>Array Processing and Wavefront Reconstruction</i>	23
3	Calibration and Target Detection	31
3.1	Range Measurement and Calibration	31
3.1.1	<i>Background Noise</i>	34
3.1.2	<i>Zero Offset and Linearity</i>	35
3.2	Bearing Measurement and Calibration.....	37
3.2.1	<i>Phase Distortion</i>	37
3.3	FFT Data Windowing and Target Detection	40
3.4	Radar Performance Results	44
3.4.1	<i>Accuracy</i>	44
3.4.2	<i>Typical Traffic Scenarios</i>	47
3.5	Ghost Targets.....	50
4	Integration with Road Geometry System	53
4.1	Problem Situations	53
4.1.1	<i>Geometric Analysis of different traffic scenarios</i>	55
4.1.2	<i>Minimum turn radius that keeps vehicle within FoV of sensor</i>	56
4.1.3	<i>Maximum road gradient</i>	57
4.2	Object Classification and Local Map	58
4.2.1	<i>Integrated System</i>	61
4.2.2	<i>Velocity setting through cruise control</i>	62
4.3	Results using Vision	63
4.4	Results using Map and GPS	70
4.4.1	<i>GPS Basic Operation</i>	70
4.4.2	<i>Digital Road-Maps</i>	74
4.4.3	<i>Integrated Obstacle and Road-Map</i>	76

CONTENTS

5 Conclusions	83
5.1 Contributions	84
5.2 Directions for Future Work	85
Appendix A	87
A.1 Derivation of Range Accuracy	87
A.2 Miscellaneous Units	89
Appendix B	91
B.1 Hardware and Software Implementation Issues	91
B.2 Timing and Optimizations on C40 DSP	96
B.3 RCS of a Corner Cube Reflector	97
Appendix C	99
C.1 Technical Specifications of Radar Sensor	99
Bibliography	101

An Integrated MMW Radar System for Outdoor Navigation

List of Figures

Figure 1.1	Navlab 5 testbed vehicle	3
Figure 1.2	Navlab 5 Harware Architecture	4
Figure 1.3	Merging obstacle and road geometry information.....	5
Figure 1.4	Evolving collision avoidance systems in smart cars . . . ?	7
Figure 2.1	Sensor Geometry	12
Figure 2.2	Sensor Area coverage	12
Figure 2.3	Triangular Frequency Modulation Waveform	13
Figure 2.4	FMCW Radar Block Diagram	15
Figure 2.5	FMCW Radar Picture	16
Figure 2.6	Antenna Horn / Lens Assembly.....	17
Figure 2.7	Antenna Diagram for Receiver Horn #2.....	18
Figure 2.8	Radar Simulation of target at (30 m, -4°).....	23
Figure 2.9	Radar Simulation of targets at (50 m, 2°) and (150m, -5°)	25
Figure 2.10	Radar Simulation of targets at (50 m, 2°) and (150m, -5°)	26
Figure 2.11	Resolution limit	27
Figure 2.12	Resolution limit of Fourier Transform.....	28
Figure 2.13	Radar resolution cell	29
Figure 3.1	Frequency increment versus Peak offset	33
Figure 3.2	Background Noise (Channel 0).....	34
Figure 3.3	Range Calibration	36

Figure 3.4	Complex FFT output.....	38
Figure 3.5	Phase Correction	39
Figure 3.6	Time domain signal and DTFT of window function	41
Figure 3.7	FFT output using same input data set, but different windows.....	42
Figure 3.8	Extended Target	44
Figure 3.9	⁽¹⁾ Range and bearing repeatability and accuracy over time	45
Figure 3.10	⁽²⁾ Range repeatability and accuracy over time	46
Figure 3.11	Radar Data for Scene 1 on Highway	48
Figure 3.12	Radar Data for Scene 2 on Highway	49
Figure 3.13	Receiver Geometry	50
Figure 3.14	Ghost targets in bearing	51
Figure 4.1	Traffic situations leading to potential false alarms	54
Figure 4.2	Road Curvatures and Sensor FoV.....	55
Figure 4.3	Minimum Turn Radius.....	56
Figure 4.4	Road gradient.....	57
Figure 4.5	Data and control signal flow diagram for integrated system	61
Figure 4.6	RALPH display for typical highway scene.....	63
Figure 4.7	Integrated <i>radar obstacle</i> and <i>vision road-map</i>	65
Figure 4.8	Tracking vehicle ahead in driving lane (Radar & Vision)	67
Figure 4.9	Tracking vehicle ahead in driving lane (Radar & Vision)	68
Figure 4.10	Tracking vehicle ahead in driving lane (Radar & Vision)	69
Figure 4.11	Differential GPS	72
Figure 4.12	GPS position error over time for stationary <i>receiver</i>	74
Figure 4.13	Digital Map of Urban Area (in Pittsburgh).....	75
Figure 4.14	Integrated <i>radar obstacle</i> and <i>GPS/road-map</i>	77
Figure 4.15	Tracking vehicles in driving lane (differential GPS).....	78
Figure 4.16	Tracking vehicle ahead in driving lane (w. carrier phase GPS)....	79
Figure 4.17	Tracking vehicles in cluttered environment.....	80
Figure B.1	Data transfer connections	92
Figure B.2	C40 software flow diagram.....	93
Figure B.3	Corner Cube Reflector	97

Basic research is what I am doing, when I don't know what I am doing.

----- Werner von Braun

Collision Avoidance and the detection of objects in the environment is an important task for an automated mobile vehicle. At Carnegie Mellon University, research in this area has been carried out in the past decade as part of the Navlab, Unmanned Ground Vehicle (UGV) and Automated Highway Systems (AHS) projects (refer to [31], [30], [9] and [10]). So far, most robotic vehicles use sonar and short range laser based sensors. For example, among many others, the GANESHA system (**G**rid **b**ased **A**pproach for **N**avigation by **E**vidence **S**torage and **H**istogram **A**nalysis) has demonstrated the use of these sensors to accomplish navigational tasks at low speeds (refer to [16] and [18]). However, the perception capabilities of GANESHA are inadequate for autonomous driving at higher speeds, both on-road and cross-country. Some perception systems have been developed, based on laser, radar or CCD cameras, to provide a longer range sensing capability and to detect obstacles. However, to date, none of these systems has demonstrated the ability to operate robustly under all weather conditions and return all the necessary geometric information about potential collision targets and safe driving directions. Problems especially still exist in cluttered environments, such as country or city roads with oncoming traffic. This thesis research therefore focuses on the following issues:

Introduction

- To build a robust, all-weather, long-range sensor with crude imaging capabilities.
- To integrate the sensor with geometric road information and vehicle state (turn arc and velocity) for an improved driving system.

The capabilities of a new sensor system will include the detection of on-road and off-road obstacles, including people, under all weather conditions, a safety monitor for lane changing and speed control with respect to traffic density.

1.1 Background and Overview

In the context of a robot automobile driving at moderate or high speeds, a sensor with a fairly long range is needed. The sensor system must be designed such that it could operate in multilane road environments together with other vehicles such as trucks, cars and motorcycles. Pedestrians are assumed to be present only in an environment where vehicles move relatively slowly. Therefore, the sensor should fulfill the following requirements:

- Maximum range between 100 and 300 meters.
- Can operate under adverse weather conditions (rain, snow).
- Can operate at night and when visibility is poor (fog).
- Data rate of about 10 Hz.
- Longitudinal resolution between 0.1 and 1 m.
- Lateral resolution must be able to discriminate between vehicles in different lanes for Highway scenario.
- Preferably no mechanically moving parts.
- Safe operation in environments where humans are present.
- No interference between different sensors.

Keeping the above requirements in mind, we decided to choose a radar-based sensor system. There are other candidates available for the sensor requirements described which are based on different physical principles. However, they have the following disadvantages for the application as compared to a radar based system:

Stereo or other video camera vision-based methods do not work well at night in general, as they depend on an external source for illumination. Owing to the structure of a CCD, they have good lateral resolution, but a good longitudinal resolution can be achieved only at relatively high computational costs. The

Background and Overview

footprint of a pixel and size of the CCD are among the factors that determine maximum range and accuracy. In order to get good resolution at long ranges, the baseline needs to be wide, which is limited by the width of the vehicle and the required overlap between the stereo images. Another problem with a stereo system is the need to mount the stereo rig rigidly onto the vehicle to avoid calibration errors. The wider the baseline, the more problematic it becomes to achieve a rigid mount. In terms of size, current stereo sensors also require a relatively large volume in space for mounting and computing.

Laser sensors are also light-based sensors. Since they emit laser light actively, they also work at night. Compared to a radar sensor, they are able to resolve smaller objects due to the smaller wavelength. However, they suffer from errors due to reflection problems from dark surfaces or mirror-like and transparent surfaces. Also, imaging lasers are currently only available using either a mechanical scanning mechanism or discrete multiple beams.

Both stereo- and laser-based sensors have problems working under adverse weather conditions especially when visibility is reduced, since they both work at visible or near-visible light wavelengths. A radar sensor exhibits much better characteristics under these conditions.

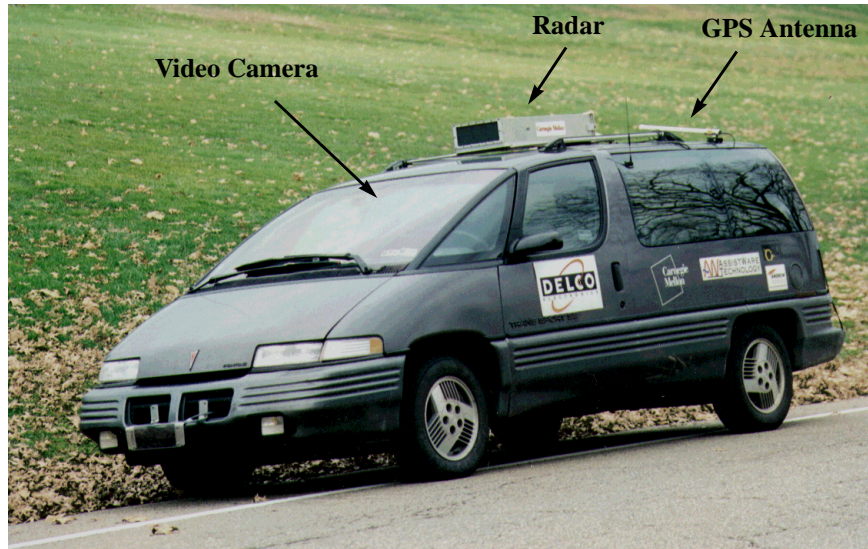


Figure 1.1 Navlab 5 testbed vehicle

Introduction

Figure 1.1 shows the Navlab 5 testbed vehicle on which most of the experiments were conducted. This vehicle is equipped with a variety of sensors. A small video camera, mounted behind the rearview mirror, is used for road following research. GPS, a yaw rate gyroscope and optical wheel encoders are available to estimate vehicle position. Steering can be computer actuated via an electric motor mounted on the steering column. Computer actuated velocity control is currently only available through the cruise control mechanism, i.e. acceleration is possible, but no braking, only coasting is available. Figure 1.2 shows the computing hardware architecture of Navlab 5.

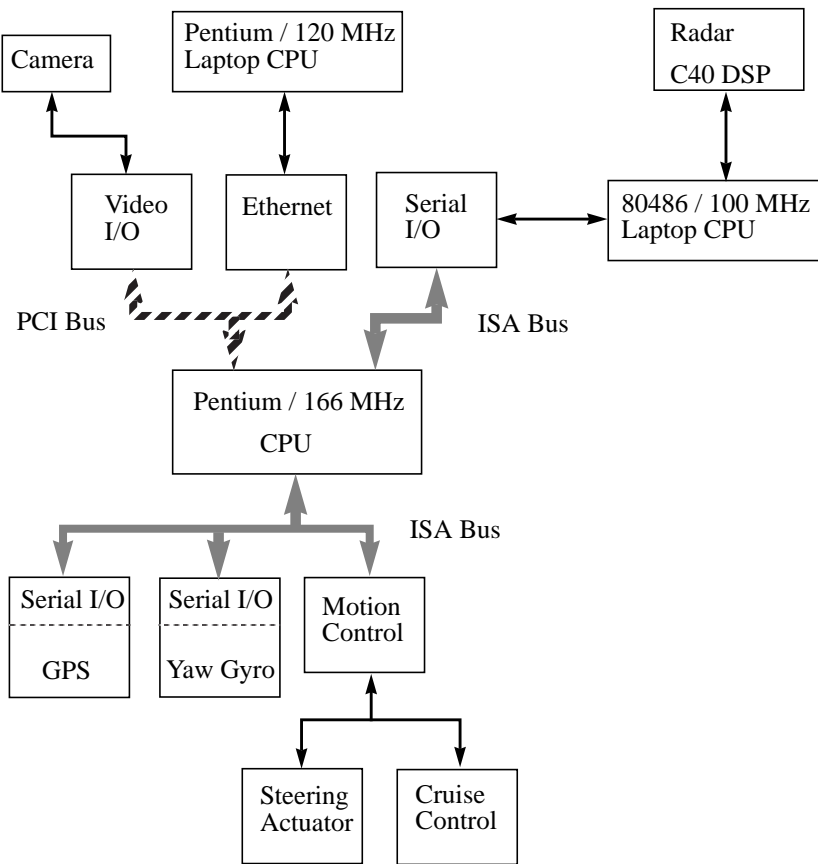


Figure 1.2 Navlab 5 Harware Architecture

A Brief History of Radar

The overall goal of this thesis research was to develop a sensor system, capable of detecting obstacles and assessing the danger-of-collision level for our own vehicle in a given traffic situation. This also requires road geometry information which is merged with obstacle location information. A typical result is shown in Figure 1.3, where obstacles detected by the radar sensor are assigned to their respective road lanes. Squares indicate radar targets automatically classified in the left lane; triangles indicate radar targets automatically classified in the right lane.



Figure 1.3 Merging obstacle and road geometry information

1.2 A Brief History of Radar

Radar cannot be attributed to a single inventor or group of inventors. Its basic concepts have been understood as long as those of electromagnetic waves. The physicist Heinrich Hertz tested Maxwell's theories experimentally in 1886 and proved that radio waves were similar to light waves and could be reflected from solid objects. Evolving from the search for a means of detecting radio waves from ships, the first patent for a radar-like system was granted to the German engineer Christian Hülsmeier in 1904. However, the idea was not seriously considered until 1922, when the Italian engineer Guglielmo Marconi presented a paper on radio detection which was subsequently tested by the United States Naval Research Laboratory. The researchers were able to detect a wooden ship passing between a transmitter and receiver, using a five-meter continuous wave radar. This type of radar is now called a

Introduction

bistatic continuous wave (CW) radar as opposed to a monostatic CW radar in which both transmitter and receiver are located at the same point. Pulse modulation as a means of measuring distance was first developed in the United States in 1925.

Radar research and development continued during the 1930s in Great Britain, France, Germany and the US. Bistatic CW radar could detect the presence of a target but not its location. Pulse radar promised a solution to this problem and a 28.3 MHz system was developed in 1936 with a range of 11 km.

From the mid 1930s through the 1940s, radar development was primarily driven by the war efforts in World War II. Germany deployed a 600 MHz radar that provided sufficient accuracy to direct effective anti-aircraft fire. In order to be able to locate objects more precisely, it is important to have a narrow radar beam. Researchers in Great Britain decided that a logical approach to narrowing radar beams was to employ higher transmitter frequencies. However, these were not available until a breakthrough occurred in 1939 with the development of the multicavity magnetron which was able to produce 20 kW of power at 3 GHz. Microwave radar became thus practical for the first time. Work continued in Great Britain and the United States on aircraft and ship detection / tracking radars in S-band (3 GHz) and X-band (10 GHz).

At the same time, another program, aircraft navigation, also began in early 1941. The name LORAN (**L**ong **R**ange **N**avigation) was adopted for this system.

After World War II, radar development continued in military as well as civilian applications. Early warning ballistic missile radars moved back to lower frequencies in the UHF range as this enabled higher transmitter power and longer detection distances up to 4,800 km. Since UHF antennas are much larger than microwave antennas, they could not be rotated but had to be fixed in place. Instead, a phased array antenna was used where the beam is steered electronically.

Radar applications also moved into terrain mapping, radio astronomy and weather radar. As an example, Synthetic Aperture Radar (SAR) is able to map large areas of terrain with high resolution images.

Although the Doppler principle was known before World War II, it was not used in radar until the 1950s. Moving Target Indicator (MTI) radar separates a target echo of a moving plane or object from stationary ground clutter. Also, small portable units of continuous wave doppler radars were developed for measuring vehicle speeds (police radar) and in the military area for detecting moving tanks, trucks and people at short ranges (approximately 100 meters).

(The above section is a summary of information taken from the Encyclopaedia Britannica. Additional information can be found in [7].)

1.3 Related Work

For nearly 20 years, companies have been developing automobile vehicle-based radar systems. Bendix developed a 36-GHz, frequency-dplexed, braking system in 1974. In the same year, Toyota and Nissan were experimenting with short-range 10-GHz radar for airbag deployment. In 1977, RCA developed a 22.5-GHz, linear frequency-modulated continuous-wave (FMCW), braking / mitigation radar, while SEL / Daimler-Benz was developing a 35-GHz, FMCW, warning radar and Nissan Mitsubishi was developing a 24-GHz pulse / doppler radar. In the 1980s, carrier frequencies moved into the 50, 60, 80, 77 and 94-GHz ranges as the required transmitter components became available.

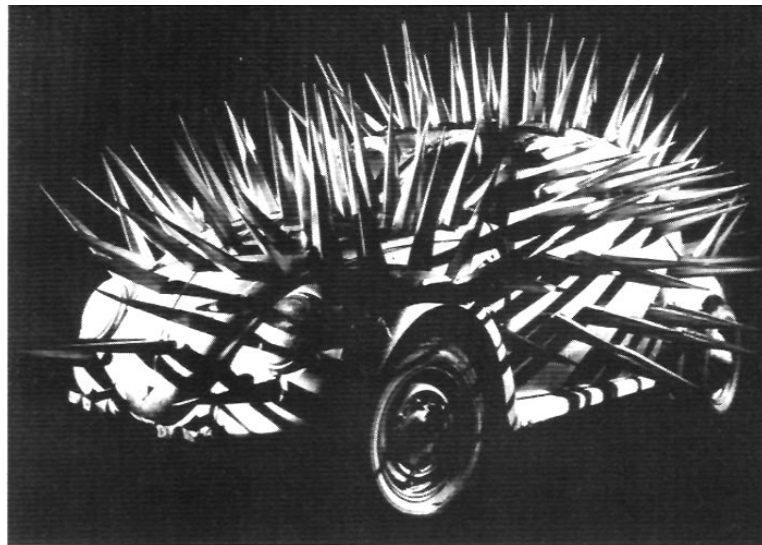


Figure 1.4 Evolving collision avoidance systems in smart cars . . . ?

With the recent advance of MMIC (**Millimeter wave Monolithic Integrated Circuits**) technology, as opposed to standard wave guide, systems also became more compact. Other companies that are currently developing radar-based systems for intelligent cruise control and collision avoidance applications are Mercedes-Benz, Vorad, Millitech, TRW, Delco, GEC Plessey and Phillips. Most of these systems use a single narrow beam sensor to detect other vehicles in the vehicle's own driving lane.

Introduction

Millitech developed a pulsed three-beam system with a total Horizontal Field of View (HFoV) of 6° . The outer beams are used to distinguish between a strong target in an adjacent lane and a weak target in the vehicle's own lane. The Vorad radar (formerly RCA) uses the doppler range method. This means that a range measurement can only be obtained when there is relative movement between sensor and target. All of these sensors potentially have problems locating a target properly in curves. Delco is currently testing an FMCW radar with a 12° field of view, using a mechanically-scanned antenna to give bearing information.

At the Technical University Munich (TUM), an automotive radar with a 12° HFoV and an operating range of 20 to 100 m has been developed [25]. Range is obtained through binary phase coding with pseudo random noise and a range resolution of 0.75 m. This radar also returns directional information through wave front reconstruction with an array of multiple receivers.

In the last 10 years several other sensor systems have been developed, using different approaches, for collision avoidance in automobiles. Mercedes-Benz and Dickmanns/Graefe *et al* equipped their vehicles with video cameras for road-following and obstacle-sensing. Other automobiles and their range are detected from a single video image, using a car model and relative size of the object in the image. Recently, one of their test vehicles was equipped with 18 video cameras looking in all directions. In this way, also objects on the side and coming up from behind are sensed.

Leica has developed an infrared laser range system. The multibeam version (MSAR Odin) uses five beams and covers a total Horizontal Field of View (HFoV) of 7.5° with a max. range of 150 m. Mercedes-Benz equipped one of the *Prometheus* vehicles with this sensor and integrated it into an intelligent cruise control. When traveling through a bend, the system uses steering angle information to focus on objects detected by the outermost sensor beams and filters stationary objects.

A simplified single beam version (Odin II) has a HFoV of 3° with an operating range of 20 to 80 m. Distance accuracy is about 3 m.

1.4 Thesis Outline

CHAPTER 1 has introduced the problem framework that was the basis of this thesis research, given some background information and discussed related work. CHAPTER 2 presents the theory and a simulation of our sensor design concept and derives the theoretically expected performance parameters of the radar sensor system.

CHAPTER 3 discusses the practically achieved radar performance parameters as given in the previous chapter, necessary calibration procedures, target detection and

Thesis Outline

provides an error analysis. CHAPTER 4 presents problematic traffic situations for a stand-alone radar sensor and discusses improved results obtained by the integration of two different road geometry systems, one of which is vision-based, the other GPS / road-map based. CHAPTER 5 summarizes the work and contributions presented in this thesis and includes directions for future research.

For a good general introduction to *RADAR* , I suggest reading reference [6] . Many derivations in CHAPTER 2 are based on this book. Overall, I have selected references that provided useful information for this research, and that I found to be most helpful to a reader without much prior working knowledge about *RADAR* and millimeter waves. Many more references are available, but information in these is mostly redundant.

Introduction

Fooling around with alternating current is just a waste of time. Nobody will use it, ever. It's too dangerous. Direct current is safe.

----- Thomas Edison

This chapter describes the field of view geometry and derives the theoretically desired parameters of the radar sensor. Many of the formulae used here are taken from [6]. We discuss the resulting hardware design and show a simulation of the required signal processing and results obtained.

2.1 Geometry

The geometry of the radar sensor design is shown in Figure 2.1. A vertical field of view of 3° was chosen as it provides a good compromise between good obstacle coverage in the vertical direction, and avoiding false measurements due to ground reflections and returns from road signs or other structures located overhead. At longer ranges, the ground (road) will reflect specularly. The current design shows a horizontal field of view of 12° , which is divided into four angular resolution cells (see also section 2.3). Assuming an average highway lane width of 4 meters, the sensor will provide an area coverage in the horizontal plane as shown in Figure 2.2. One lane will be covered at a range of approximately 19 meters and three lanes will

Sensor Design Concept

be covered at a range of 57 meters. At a range of 95 meters the sensor covers an area of 20 m by 5 m in the vertical plane. A 3° angular resolution cell covers an entire lane width at a range of 76 meters.

It would have been preferable to use a larger horizontal field of view of up to 20° . However, for cost reasons in the antenna design, we settled on the HFoV shown.

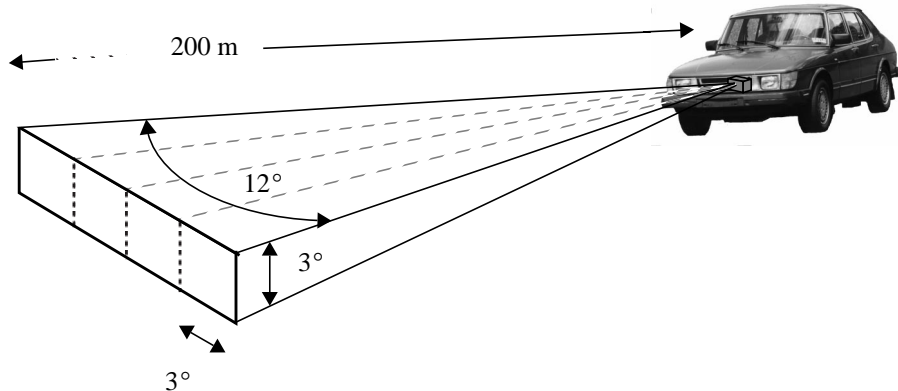


Figure 2.1 Sensor Geometry

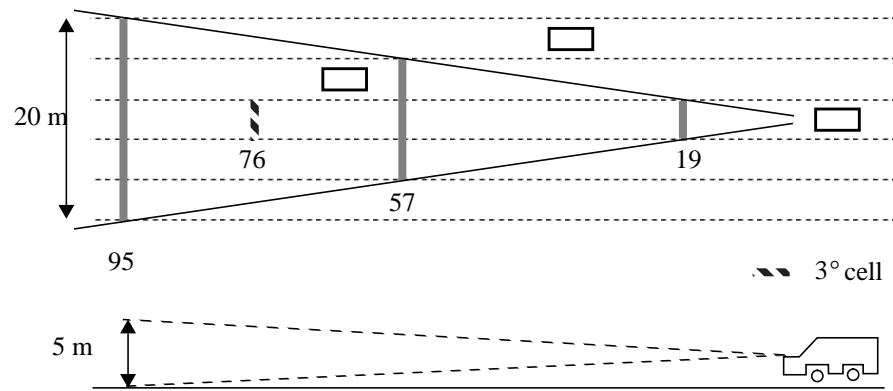


Figure 2.2 Sensor Area coverage

Radar Specifications

In order to stop for a stationary object at highway speeds of 100 km/h (~ 65 mph), a detection distance of at least 55 metres would be needed (assuming $a = -7 \text{ m/s}^2$ and neglecting reaction time). Since, in autonomous mode, the vehicle needs to react to objects moving at considerably different relative speeds, the maximum range of the sensor for detecting vehicles is designed to be about 200 meters. People have a much lower radar cross section ($0.2 - 2 \text{ m}^2$) as compared to vehicles (10 m^2) and can therefore be detected only at a much smaller maximum range. For the sensor system, this would be about 60 meters. However, this does not pose a problem, because people are assumed to be present only in a road environment where vehicles also move considerably slower, i.e. 50 km/h (~ 30 mph).

2.2 Radar Specifications

As described in CHAPTER 1 in sections 1.2 and 1.3, many different design options are possible for a radar in the required application. For simplicity of design and better sensitivity, we decided to operate the radar as a Frequency Modulated Continuous Wave (FMCW) system. A block diagram of the design is shown in Figure 2.4. The carrier frequency is at 77 GHz which is the emerging standard. The corresponding wavelength is 3.9 mm which results in better resolution of scene details than at lower frequencies. Above 30 GHz, reflection from vegetation and foliage is more significant.

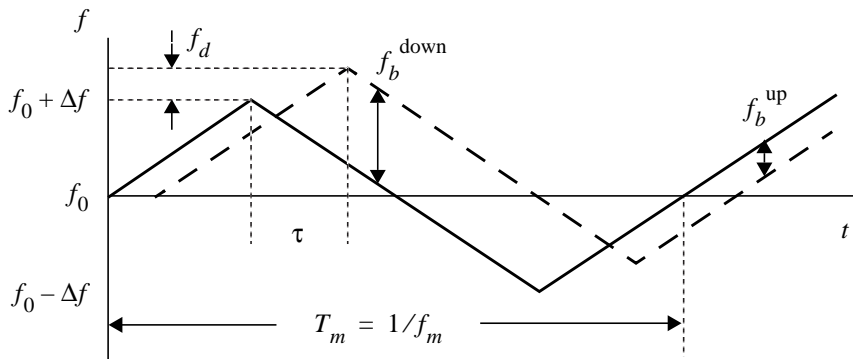


Figure 2.3 Triangular Frequency Modulation Waveform

Sensor Design Concept

Also, attenuation at these frequencies is larger than at lower ones. However, this keeps the maximum range of the radar relatively short and thus reduces interference. A carrier frequency in the millimeter wave range also allows larger frequency sweeps for better range resolution and limits interference with existing commercial radio frequency transmitters. Because the transmitted signal is spread over a large bandwidth, an FMCW radar is quite robust against interference from other sensors of the same type. Interference can be further reduced by using a coded FM wave form. Using the formulae given in [6], we can now compute the parameters for a simple radar system.

For a triangular modulation, the range to a target can be calculated by:

$$R = \frac{c}{8\Delta f f_m} \cdot \tilde{f}_b \quad (2.1)$$

where c is the velocity of light, $2\Delta f$ the frequency sweep, f_m the modulation frequency and \tilde{f}_b the average frequency difference between outgoing and returned wave on the upward and downward slope of the modulation, f_b^{up} and f_b^{down} . Frequency errors due to doppler shift f_d are eliminated as the doppler shift has opposite signs between upsweep and downsweep (see Figure 2.3).

The maximum range resolution is related to the bandwidth by the following relation:

$$\delta R = \frac{c}{2B} \quad B = 2\Delta f \quad (2.2)$$

The frequency sweep $2\Delta f$ of this radar is 300 MHz, which therefore results in a range resolution of 0.5 m. For a maximum range of $R = 200$ m and a desired maximum intermediate frequency (IF) of $f_{IF} = 500$ kHz, the modulation frequency f_m is given by equation (2.3) and is calculated to be 625 Hz for a triangular modulation and 1.25 kHz for a sawtooth modulation:

$$f_m = \frac{c \cdot f_{IF}}{8\Delta f R} \quad (\text{Bipolar Triangle}) \quad f_m = \frac{c \cdot f_{IF}}{4\Delta f R} \quad (\text{Sawtooth}) \quad (2.3)$$

If the FM waveform used is triangular, maximum unambiguous range is 1200 km and can be calculated from equation (2.4):

$$R_m = \frac{c}{2f_m} \quad (2.4)$$

Radar Specifications

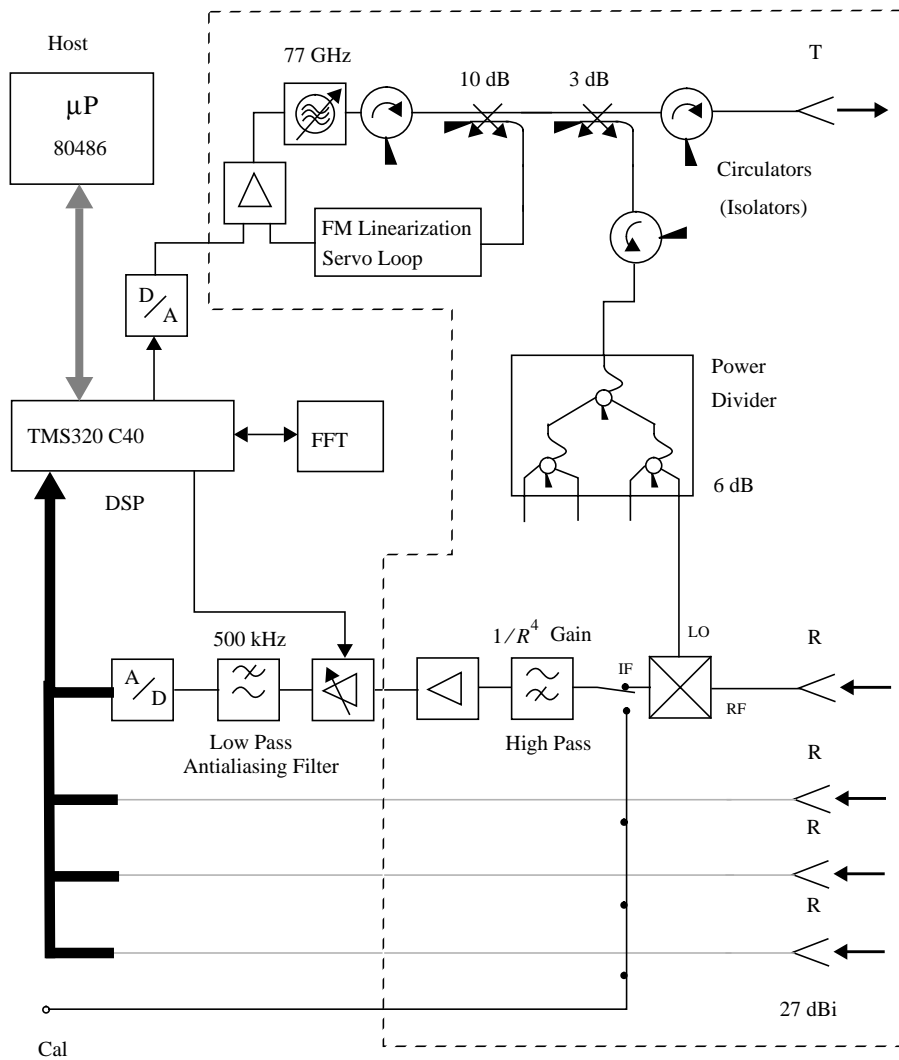


Figure 2.4 FMCW Radar Block Diagram

Sensor Design Concept

Since the measuring range is much less than the ambiguity interval of the FM and the radar has low transmitter power, no targets are detected outside the unambiguous range. Hence ghost targets due to range ambiguity are avoided. A summary of all parameters is given in Appendix C.

Finally, the doppler frequency shift due to a relative radial motion between the radar sensor and a target is given by,

$$f_d = \frac{2v}{\lambda} \quad (2.5)$$

At 77 GHz, we have a wavelength $\lambda = c/f = 3.9$ mm, which results in a doppler shift of 142 Hz per km/h relative target speed. This means for example, that the resulting range error due to doppler shift for a target moving at a relative velocity of 100 km/h (65 mph) would be 5.7 meters.

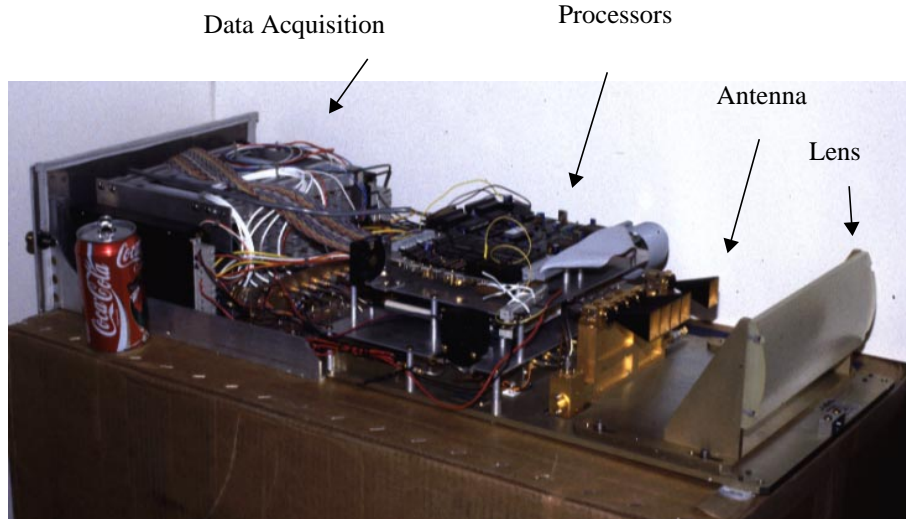


Figure 2.5 FMCW Radar Picture

2.2.1 Antenna Design and Transmitter Power

In order to be able to detect vehicles and people within the given range and geometric requirements, as discussed in section 2.1, transmitter power and antenna type need to be specified. For cost reasons we could not use a sophisticated new design, but had to take parts that were already available. Hence, we used standard gain horn antennae

Radar Specifications

with a $12^\circ \times 12^\circ$ field of view for all transmitter and receiver channels. The vertical field of view of 3° was achieved by placing a custom designed cylindrical lens in front of the antennae as shown in Figure 2.5 and Figure 2.6. We chose a cylindrical rather than a fresnel lens in order to keep sidelobes well attenuated.

For a linear aperture, the 3 dB beam angle in degrees can be calculated as,

$$\theta_{3dB} = \beta \cdot \frac{\lambda}{D} \approx 65 \cdot \frac{\lambda}{D} \quad (2.6)$$

where D is the aperture size of a single horn antenna in the plane of angle θ_{3dB} and $\beta \approx 65$ for a sidelobe level at approx. -25 dB (refer to [6] and [19]). Note that the physical aperture of a horn antenna is actually rectangular for design reasons rather than square. D describes a fictitious surface located on or near the antenna through which a major portion of the radiation passes. It corresponds roughly to actual physical aperture size. Here, $D \approx 21$ mm.

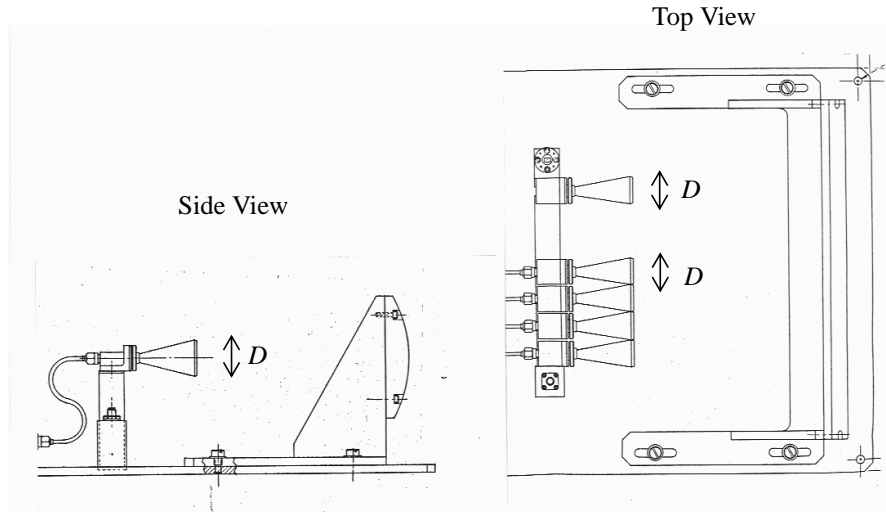


Figure 2.6 Antenna Horn / Lens Assembly

The antenna gain is given by the equation below (see [19]),

$$G = \frac{4\pi\rho A}{\lambda^2} \quad (2.7)$$

Sensor Design Concept

where A is the geometric surface of the aperture and ρ is the aperture efficiency. Taking $\rho = 0.5$ and using equation (2.6), we can estimate the approximate gain of the antenna system as (see also Appendix A),

$$G \approx \frac{27000}{\theta_{3dB} \cdot \phi_{3dB}} = 750 = 29 \text{ [dBi]} \quad (2.8)$$

θ_{3dB} and ϕ_{3dB} are the beam angles in azimuth and elevation, in degrees, respectively.

Figure 2.7 shows the antenna diagram for one of the antennae in the array. It can be seen that, in elevation, the sidelobes are quite well attenuated, i.e. better than -19 dB, whereas in azimuth (horizontal field of view) the first sidelobe is attenuated only to -9 dB. This is partly because the cylindrical lens also makes a phase correction which results in reduced sidelobes in elevation. The lens affects elevation only and thus sidelobes in azimuth are not much attenuated. An asymmetry of sidelobes in elevation could be caused by a misalignment of the optical axis of the lens with the axis of the feed horn. For a transmitted signal returned from a target, the sidelobe attenuation is the combination of transmitter and receiver antennae and will therefore be twice that shown in Figure 2.7, since all antennae exhibit the same characteristics. However, this still results in a fairly high level of sensitivity in the sidelobe area of the antenna. This means that a strong reflector in this region could potentially be detected as a target.

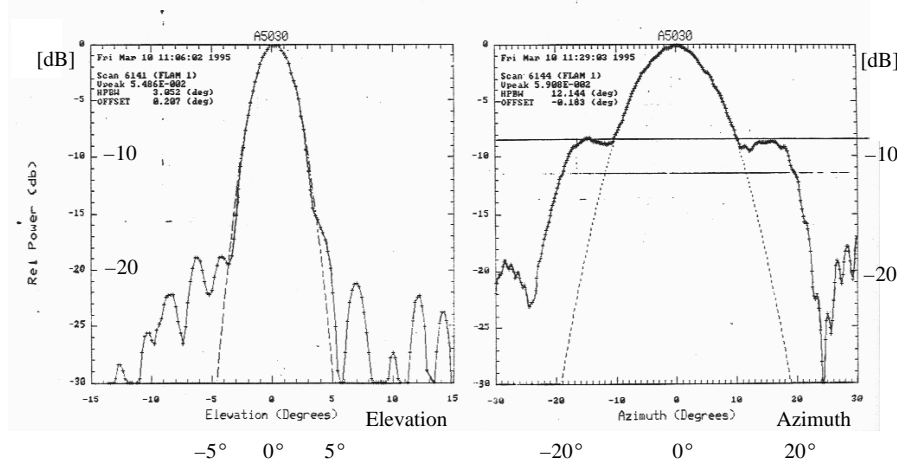


Figure 2.7 Antenna Diagram for Receiver Horn #2

Unfortunately, this happens to be a very undesirable artifact because such a target will be outside the unambiguous horizontal field of view (refer to section 2.3) and will result in a ghost target mirrored back into the valid field of view (see section 3.5). By design, horn antennae have a rectangular aperture. In order to obey the relation expressed by equation (2.18), the smaller aperture dimension has to be used for placing array elements adjacent to each other. However, this is also the plane exhibiting the worst sidelobe characteristics of the two aperture dimensions (see Figure 2.7). A better, but also much more costly, antenna design could avoid these problems (refer to CHAPTER 5, section 5.2).

We can now calculate the required transmitter power P_t from the *radar equation* (see [6], [5]) and the previously computed antenna gain in equation (2.8), in order to detect vehicles and people within the specified ranges (see section 2.1).

$$P_t = \frac{(4\pi)^3 R_{max}^2 P_{r min}}{G^2 \lambda^2 \sigma} \quad (2.9)$$

The required minimum power level at the receiver in order to detect a target is assumed to be $P_{r min} = -100 \text{ dBm} \equiv 10^{-10} \text{ mW}$ (see also Appendix A).

For detecting a person with a radar cross-section of $\sigma = 0.2 \text{ m}^2$ at a maximum range of $R_{max} = 60 \text{ meters}$, we therefore need a transmitter power of $P_t = 15 \text{ mW}$ ($G = 750$).

For detecting a vehicle with a radar cross-section of $\sigma = 5 \text{ m}^2$ at a range of $R_{max} = 150 \text{ meters}$, we need a transmitter power of $P_t = 24 \text{ mW}$.

Based on the above calculations, Federal Communication Commission (FCC) requirements and available components, we finally selected a transmitter signal power of approximately 30 mW.

2.2.2 Range and Angular Accuracy

For digitizing the analog output of the MMW radar front end, a 12 bit A/D converter is used, sampling the analog signal at 2.5 MHz. As a general rule, the Signal-to-Noise ratio (SNR) can be taken as 6 dB per bit. In the bipolar case, i.e. where the output voltage range is $\pm V(t)$, we need to subtract 6 dB in addition. Hence, the SNR of the A/D conversion computes to $12 \cdot 6 - 6 = 66 \text{ dB}$. This also corresponds roughly to the maximum dynamic range of the MMW radar front end for a strong target detected at close range. Typically, however, the SNR for a real target signal detected at longer ranges is around 30 dB (see Appendix A).

Sensor Design Concept

In [28], an expression is derived which relates the theoretical rms angular error to wavelength, aperture length and Signal-to-Noise ratio (SNR), and is given by,

$$\delta\alpha_{rms} = \frac{\lambda}{L \sqrt{2} \text{ SNR}} \quad (2.10)$$

where SNR is in linear units and in terms of signal powers instead of dB (see Appendix A).

The radar has four receiver elements with the spacing between adjacent elements given by equation (2.18). Substituting in equation (2.10) and using array length $L = 4\Delta x$ as shown in Figure 2.8, we then obtain

$$\delta\alpha_{rms} = \frac{\sin(2\theta_u)}{4 \sqrt{2} \text{ SNR}} = \frac{\sin 12^\circ}{4 \sqrt{2 \cdot 10^{30/10}}} = 1.16 \text{ [mrad]} \quad (2.11)$$

where $2\theta_u = 12^\circ$ is the unambiguous horizontal field of view (refer to section 2.3) and $\text{SNR} = 30 \text{ [dB]}$. Thus, the theoretical angular error for a single point target calculates to 1.16 mrad or 0.066 degrees.

Similarly, we can compute the theoretical rms range error for a single point target as derived in Appendix A:

$$\delta R_{rms} = \frac{c}{4\Delta f \sqrt{2} \text{ SNR}} \quad (2.12)$$

For a frequency sweep of $2\Delta f = 300 \text{ MHz}$, we obtain $\delta R_{rms} = 1.12 \text{ cm}$.

It should be noted, however, that most real objects are not point scatterers, and target smearing owing to multiple reflectors on a single extended target will certainly affect accuracies. Also, because of the particular reflective properties of radar, the Signal-to-Clutter S/C ratio in a given radar system is usually a more dominant factor in determining obtainable accuracies than Signal-to-Noise ratio (SNR). S/C depends on wavelength, illuminated area and the geometry of the targeted environment. It therefore needs to be determined empirically.

Range and angular information of targets are obtained by Fast Fourier Transform (FFT), as described in the following section.

2.3 Signal Processing

The output of the mixers on the receiver channels of the radar sensor (see Figure 2.4) is a mixture of different frequencies. Each discrete frequency corresponds to range to a target. Therefore, the range to a target can be obtained efficiently by using a FFT. The received signals are first passed through a high pass filter which acts as a range dependent gain, since signal frequency corresponds to range. The signals are then amplified and fed through a low pass filter at 500 kHz before being converted to digital. The low pass filter prevents errors due to aliasing effects in the succeeding FFTs.

2.3.1 FMCW Radar Simulator

We implemented a simple simulator of the FMCW radar for testing different signal processing algorithms. These algorithms are used to extract range and bearing information from the mixer output signals of the receiver channels (see Figure 2.4). The basis of the simulator is the generation of the ‘expected’ mixer output signals, given an ideal simulated target at a particular range and bearing location. The simulation model uses only geometric information of relative locations of radar sensor and target and the resulting time delays of the transmitted wave fronts. Multiple targets can be simulated.

We assume that the transmitted wave front is a sinusoidal signal with a unit amplitude $S_T(t) = \sin(\omega t)$. The output of a mixer is then the product of the transmitted signal and the time-delayed, received signal from the antenna $S_R(t) = S_T(t - \tau)$ (refer to Figure 2.4 and [6]),

$$\begin{aligned} S_{Mx}(t) &= S_T(t) \times S_R(t) \\ &= \sin \omega t \cdot \sin \omega (t - \tau) \\ &= \frac{1}{2} \cos (\omega t - \omega (t - \tau)) - \frac{1}{2} \cos (\omega t + \omega (t - \tau)) \end{aligned} \tag{2.13}$$

where τ is the time delay proportional to range to target.

As can be seen in equation (2.13), $S_{Mx}(t)$ contains the IF frequency in the lower side band and an image frequency in the upper side band. As the carrier and higher frequencies are removed by the mixer through a low pass filter, the baseband (IF) signal remains as the mixer output,

$$\begin{aligned}\overline{S_{IF}}(t) &\equiv \frac{1}{2} \cos(\omega t - \omega t + \omega \tau) \\ &= \frac{1}{2} \cos \omega \tau\end{aligned}\tag{2.14}$$

Absolute signal phase locked to the carrier ωt has been neglected here as it cancels anyway in equation (2.14). The above equation shows that if the radar operates in CW mode only, without modulation of the carrier, the resulting mixer output will be a DC offset. However, if we add a frequency modulation of the carrier, then ω is not a constant anymore. For simulation purposes we discretize the function with respect to time-frequency for one modulation period T_m and then can rewrite equation (2.14) as,

$$\begin{aligned}S_{IF}[i] &= \frac{1}{2} \cos(2\pi \cdot i \cdot f_{FM} \cdot \tau) \\ \text{where } (f_0 - \Delta f) &\leq i \cdot f_{FM} \leq (f_0 + \Delta f) \\ \text{for } 0 &\leq i \leq T_m\end{aligned}\tag{2.15}$$

For a receiver array, τ will slightly vary across receiver channels for a particular target, as the relative signal phase between channels will vary depending on target bearing (refer to section 2.3.2 for a detailed explanation). Hence, τ depends on target range and bearing. For receiver channel k , it can be expressed as,

$$\tau \equiv \tau_k = \frac{2R}{c} + \frac{k \cdot \Delta x \sin \alpha}{c} \quad k = 0 \dots 3\tag{2.16}$$

where R and α are range and bearing of the simulated target respectively (refer to Figure 2.8 (a)). Equations (2.15) and (2.16) are then used to generate the desired simulated IF signal as mixer output.

2.3.2 Array Processing and Wavefront Reconstruction

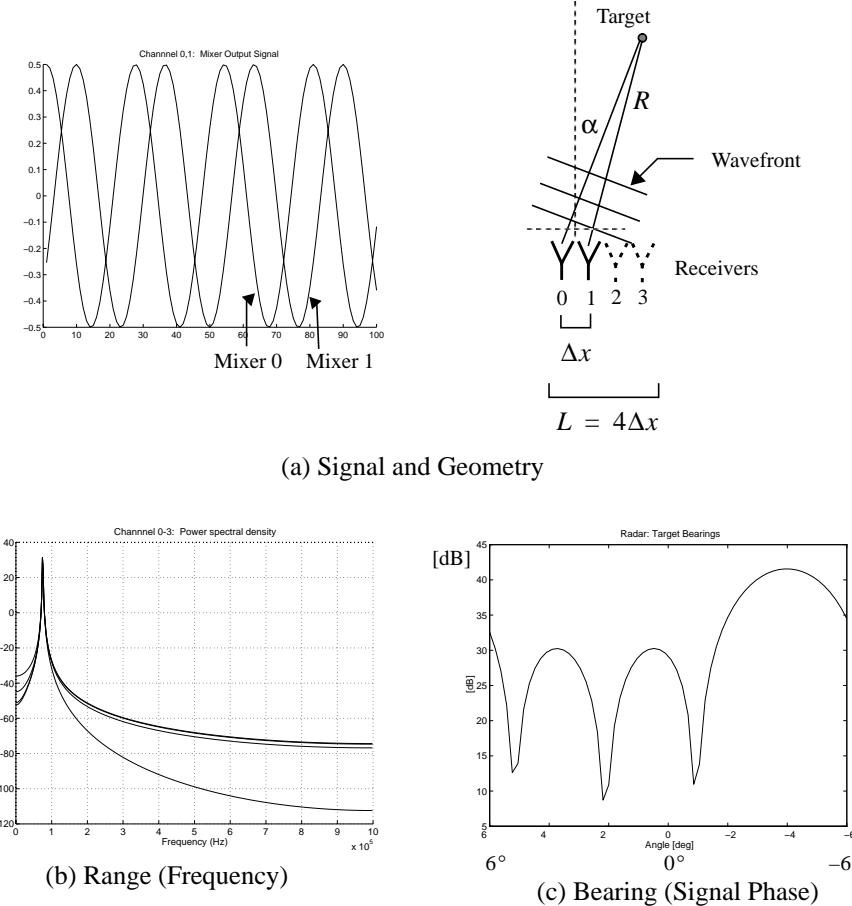


Figure 2.8 Radar Simulation of target at (30 m, -4°)

Angular bearing of the target is obtained by digital wave front reconstruction and beam forming. This involves two consecutive FFTs along the time and space dimension of the signal. The space dimension is in this case the four receiver elements that are used to sample the incoming wave front at discrete points in space. The basic idea is shown in Figure 2.8 for a simulated target at (30m, -4°);

demonstrated on two out of the four receivers shown. A parallel wavefront reflected from a target, offset from the major sensor axis, is incident at an angle on the receiver array. As can be seen in this case, the wavefront arrives slightly earlier in time on receiver 1 than on receiver 0. Thus, there is a small difference in range which results in a slightly different frequency output between receivers. This small frequency difference cannot be resolved by the FFT in range, but it shows up as a phase difference in the time signal (Figure 2.8 (a)).

A mathematical description of the signal and associated phase (time) lag for receiver channel k and target j can be expressed by (see also section 2.3.1),

$$\begin{aligned} S_{jk}(t) &= A \cos(\omega_j t + \phi_{jk}) \\ &= A \cos(2\pi f_j(t - \rho_{jk})) \end{aligned} \tag{2.17}$$

$$\text{where } \rho_{jk} = \frac{k \cdot \Delta x \sin \alpha_j}{c} \quad k = 0 \dots 3$$

Phase lag is relative to channel 0 which is also denoted as the origin of the receiver array.

The first FFT along the time dimension of the receiver output signal now gives target range as mentioned above and relative phase information. The second FFT along the space dimension performs a cross correlation that is a measure of the phase (time) lag between the signals in each receiver channel. The maximum peak in the correlation indicates the phase (time) lag and, thus, the bearing of the incoming signal (Figure 2.8 (b)). Since there are only four data points from the four receivers, additional bins are zero padded to 256 in order to increase accuracy.

A more detailed description of the method is given in [1] and [2]. Since the radar has four receivers, we obtain four angular resolution cells as shown in Figure 2.1. In order to determine target bearing unambiguously within the given sensor's field of view, the following condition for the receiver antenna spacings Δx_i needs to be obeyed, as determined by the sampling theorem:

$$\Delta x_i \leq \frac{1}{\sin(2\theta_u)} \cdot \lambda \tag{2.18}$$

where $2\theta_u = 12^\circ$ is the unambiguous angular range, i.e. the horizontal field of view. In order to be able to use Fourier Transform processing techniques, the sampling points must be evenly spaced either in the time or spatial domain. Thus we use equal antenna spacings $\Delta x_i = \Delta x$ for $i = 1 \dots 4$ for a receiver array of aperture size (length) $L = 4\Delta x$.

Signal Processing

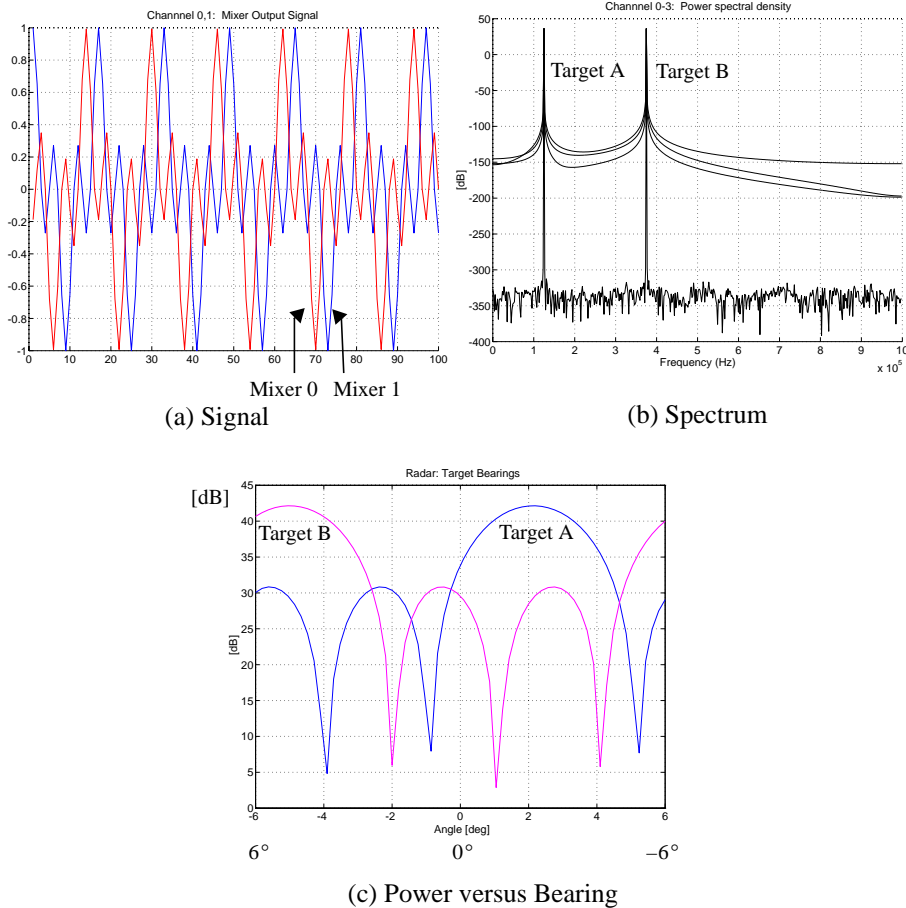
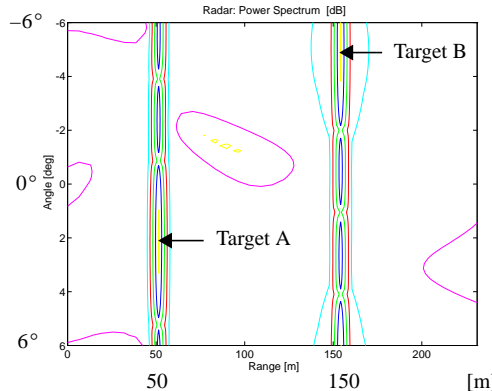


Figure 2.9 Radar Simulation of targets at (50 m, 2°) and (150m, -5°)

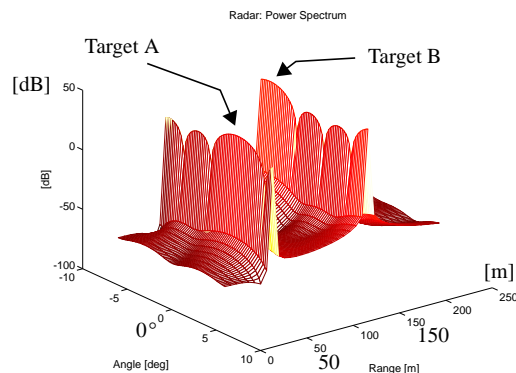
Figure 2.10 and Figure 2.10 show the radar signal processing for two simulated targets at (50 m, 2°) and (150m, -5°):

(a) shows the overlaid time signal from the output of two of the four mixers. Note that the range information is contained in the frequency and the bearing information in the phase shift of the signals.

Sensor Design Concept



(d) Contour Plot of Range / Bearing Matrix



(e) Mesh Plot of Range vs. Bearing Matrix

Figure 2.10 Radar Simulation of targets at (50 m, 2°) and (150m, -5°)

(b) is the spectrum of the fourier transformed time signals for 1024 data points. The four spectra from the mixers are overlaid. The noise level at -350 dB is just numerical noise in channel 0. The noise level in channels 1-3 is much higher due to leakage effects in the FFT. In this simulation, we did not introduce any system noise but only used ideal signals.

(c) is a cross-sectional cut through the range vs. bearing matrix at the calculated range for target A and target B. The difference in level between the mainlobe and the first sidelobe is 11.5 dB, as predicted by theory [1].

(d) shows a contour plot of the range vs. bearing matrix after both FFTs are applied along range and bearing dimension. In the range dimension we used 256 data points. In the bearing dimension we used 64 bins, zero padded from the four data points. The peaks indicating targets A and B can be seen at their expected locations.

(e) shows a mesh plot of the same range vs. bearing matrix as in (d).

All simulations were implemented using the MATLAB software package.

Ideally, a Fourier transformation of a sinusoidal signal in the time domain results in a Dirac function in the frequency domain. However, since we have to use a finite sample time, the continuous time signal is essentially convolved with a rectangular window when applying the Fourier Transform [8]. This results in a widening of the dirac function into a sinc function ($\sin x/x$) which limits the resolution ability of the FT. According to the Raleigh criterion, two targets are considered distinctly resolved if their separation is such that the peak of the mainlobe of one target falls on the first minimum of the other target, or greater (see Figure 2.11).

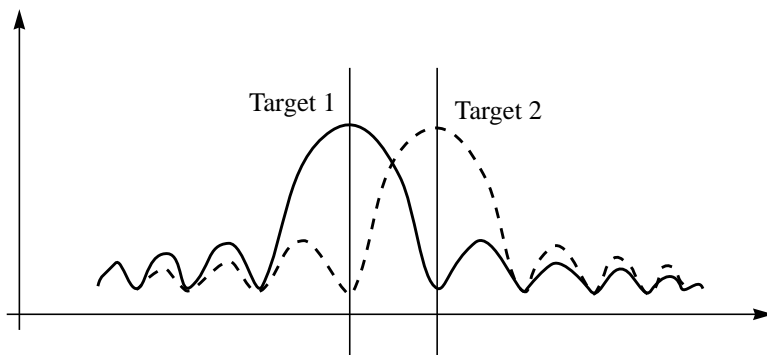


Figure 2.11 Resolution limit

Sensor Design Concept

The width of the mainlobe and hence resolution ability depends upon the number of data points available for the Fourier Transform. This means that, for the bearing dimension, one resolution cell is $12^\circ / 4 = 3^\circ$, since we have four receivers in the spatial dimension to sample the incoming wavefront. Hence, if two targets are at the same range but their bearing is less than 3° apart, they cannot be resolved anymore and are merged into one target lobe. This situation is illustrated in Figure 2.12: In (a), the targets are 3° apart and can just be resolved; In (b) the targets are less than 3° apart and cannot be resolved anymore.

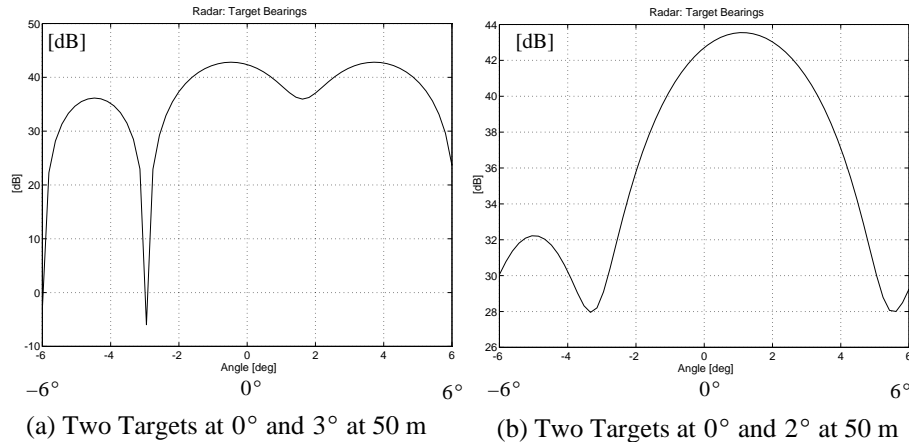


Figure 2.12 Resolution limit of Fourier Transform

It should be noted that here resolution is the ability of the system to distinguish between two separate targets that are close together, whereas accuracy is the absolute accuracy with which a single target position can be determined. Accuracy, but not resolution, can be increased by zero padding.

If multiple reflectors are present within a radar resolution cell, then each reflector contributes some amount to the total reflected signal from that resolution cell. Since individual reflectors cannot be resolved within a resolution cell, the combined signal is the vector sum of all reflector contributions. For reflectors distributed at spatially different locations throughout the cell, the measured target position in that cell is thus located at the centroid of all individual contributions (see Figure 2.13). Thus, a single weak reflector next to a strong reflector influences actual target location only by a small amount. However, a large number of weak reflectors could potentially drown out the signal from a strong single target reflector.

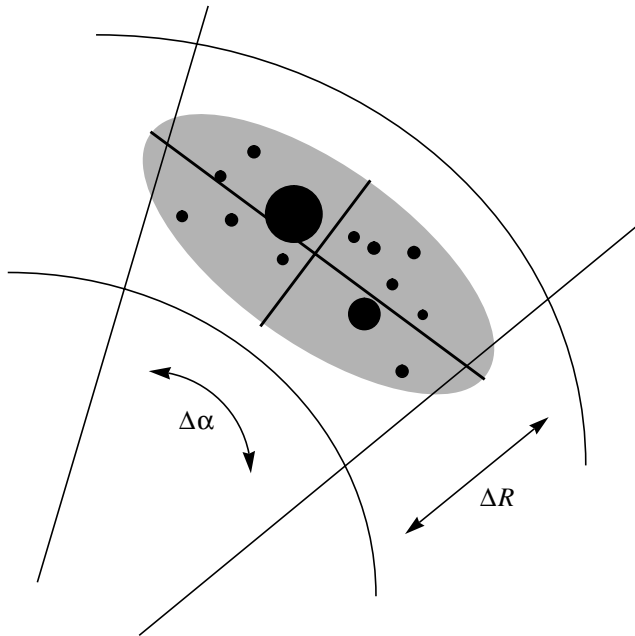


Figure 2.13 Radar resolution cell

Therefore an increased resolution is generally desirable as it leads to an improved Signal-to-Clutter S/C ratio. This improvement occurs because ground and rain clutter generally fill an entire radar resolution cell, but the dimensions of a typical radar target are usually much smaller.

Finally, it should be mentioned that target resolution could also be increased by using a ‘High Resolution Spectral Estimation’ method, such as MEM or Extended Prony. Many of these methods are described in [1], [3], [11], [12] and [20]. The advantage here would be that a performance improvement could be achieved without any expensive hardware modifications. We looked at a variety of these methods, but decided at this point not to pursue it as most of them are computationally quite expensive which makes a real time implementation difficult. In addition, many of them do not operate quite as robustly in the presence of noise as compared to a Fourier Transform (see also CHAPTER 5, section 5.2).

Sensor Design Concept

It is a capital mistake to theorize before one has data.

----- Arthur Conan Doyle

In CHAPTER 2 we described the theoretical parameters of the radar sensor system. In a real system these are not necessarily attainable because of the influence of noise and drift over time from a variety of sources. In this chapter we will show the calibration procedures used in order to obtain the required system performance and also discuss some experimental results.

3.1 Range Measurement and Calibration

The range to a target is obtained by Fourier transforming the digitized signal of the four receiver channels (Figure 2.4). The value in each FFT cell is then averaged over all four channels in order to improve the signal-to-noise ratio. A peak in the FFT output indicates the presence of a target. Hence, the associated frequency and related target range can be computed from the FFT bin i as follows:

$$\begin{aligned} F &= \frac{i \cdot \Delta F}{N} \\ R &= \frac{F}{K} - R_{off} \end{aligned} \tag{3.1}$$

where $\Delta F = 2.5$ MHz is the sampling frequency for digitizing the signal, $N = 1024$ or 2048 is the total number of samples taken, $K = 2.30$ [kHz / m] is a system constant and R_{off} is the zero range offset.

In order to obtain correct range readings, we must calibrate K and R_{off} which is described in section 3.1.2. .

As equation (3.1) shows, the width of an FFT bin determines the accuracy with which the range of a target can be determined so far as it does not reach the theoretical limit. (The difference between accuracy and resolution and their theoretical limits are discussed in CHAPTER 2.)

For our radar in the case of $N = 1024$, the accuracy is approximately one meter. We can improve the accuracy by zero padding the FFT and thereby evaluating the signal on a finer frequency grid. However, this approach is computationally expensive. A simpler method is given as follows: due to the discrete sampling of the analog signal, we have *leakage* effects when applying a FFT (refer to [8], [11] and [24] for a more detailed explanation). If the signal frequency to be analysed falls exactly into a frequency bin of the FFT, there is no leakage and the FFT output is a strong peak at this location. However, in most cases, the exact frequency of the input signal falls somewhere between two FFT frequency bins. This results in a leakage of signal power into neighbouring bins which may be substantial. The amount of signal power leaked depends upon how far off center the actual signal frequency is. We therefore approximate the sinc function due to a target in the FFT output, by fitting a parabola at the maximum to three points. These are the center bin which contains the peak and the two adjacent bins. Thus, we can obtain a more accurate estimate of the actual location of the peak. An even better estimate could probably be obtained by generating a look-up table of sinc functions, but we decided to use the parabolic approximation for simplicity and since the obtained accuracy turned out to be sufficient for our application.

Using the equation for a parabola with the vertex on the x-axis and focus on the negative y-axis,

$$(x - x_0)^2 = -4a \cdot y \tag{3.2}$$

we can now derive an expression for calculating the peak offset within one FFT bin x_0 in the interval $[-0.5, 0.5]$:

$$r_0 = \sqrt{\frac{P_{max} - P_{max-1}}{P_{max} - P_{max+1}}} \quad (3.3)$$

$$x_0 = 0.5 \cdot \frac{r_0 - 1}{r_0 + 1}$$

Equation (3.1) has to be modified accordingly:

$$F = \frac{(i + x_0) \cdot \Delta F}{N} \quad (3.4)$$

Figure 3.1 shows frequency increments versus x_0 within one FFT bin for a simulated signal. The center frequency in this case is 104.9 kHz.

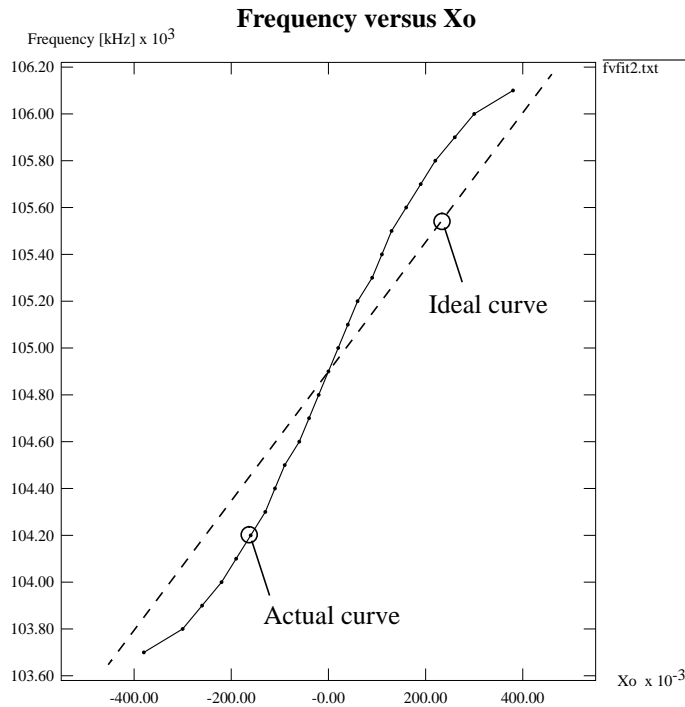


Figure 3.1 Frequency increment versus Peak offset

With this method, we can achieve approximately ten times an improvement in accuracy without too much computational effort. Thus, if the FFT bin separation equals one meter, we can obtain an accuracy of approximately 10 cm. Again, this is true only for a point target, but not necessarily for an extended target with multiple reflectors within a single resolution bin (see also section 2.2.2).

3.1.1 Background Noise

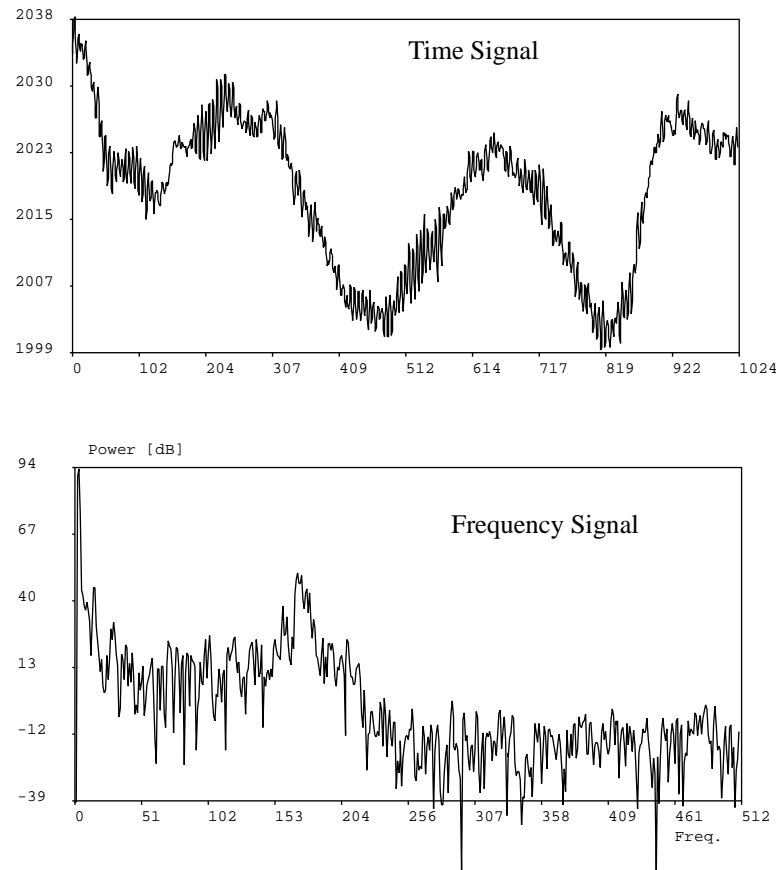


Figure 3.2 Background Noise (Channel 0)

Background noise is always present in any radar system and can be produced by a variety of sources. There could be an inductive coupling of frequencies generated by the system that could lie within the IF bandwidth. Therefore, in this case great care had to be taken when designing the system that all frequencies in the range 10 – 500 kHz were eliminated. Another source are the mixers and cross-coupling between receiver channels and transmitter. Also, part of the transmitted signal energy is reflected back from the rear portion of the lens and shows up in the IF as a low frequency signal. On the A/D side, the DC offset of the signal should ideally be zero in order to avoid a large peak with sidelobes in the DC bin of the FFT.

In order to remove the influence of these noise sources, the following procedures are used:

The remaining DC offset is removed in software by subtracting the average of the signal from the signal in each channel before the FFT.

The background noise is then estimated by taking a data sample with no reflectors present, i.e. either by putting an absorber in front of the antenna or by pointing the sensor into the sky. This data sample then constitutes the calibration data set as shown in Figure 3.2. Note that the digitized time signal is 12 bit, i.e. range

0 – 4095 . In general, each contribution of a target to the sensor output (FFT periodogram) can be viewed as a statistically independent process. In this case we can subtract the calibration data set from the sensor output.

Because of sidelobe leakage effects and fluctuating target intensities, the actual threshold for detecting a target has to be set slightly higher than zero in order to avoid numerous false alarms.

3.1.2 Zero Offset and Linearity

In order to obtain correct range readings, we also must calibrate K and R_{off} (see equation (3.1)). K is a system constant that depends on the slope of the FM sweep and gives the frequency increment per FFT frequency bin in kHz per meter. For collecting the calibration data we used a corner reflector as target and a laser range finder (pulsed) to measure the actual reference range to the target. The laser range finder had an accuracy of about 10 cm which was sufficient for this purpose. Note that K and R_{off} have to be recalibrated if the modulation waveform is changed.

Figure 3.3 shows a plot of actual range (laser) versus measured range (radar) for several data points taken between 18 and 109 meters, relative to the antenna lens. We can observe that the relation between actual and measured points is fairly linear. Hence by fitting a straight line $y = mx + c$ to n data points we can determine the range offset R_{off} as the intercept on the y-axis. Using the equations for a least square fit we get,

$$m = \frac{n \sum x_i y_i - (\sum x_i)(\sum y_i)}{n \sum x_i^2 - (\sum x_i)^2} \quad (3.5)$$

$$R_{off} = c = \frac{\sum y_i}{n} - m \frac{\sum x_i}{n} = 2.9 \text{ [m]} \quad (3.6)$$

$$\text{Standard Error} = \sqrt{\frac{\sum [y_i - (c + mx_i)]^2}{n - 2}} = 0.325 \text{ [m]} \quad (3.7)$$

Uncalibrated Range versus Actual Range

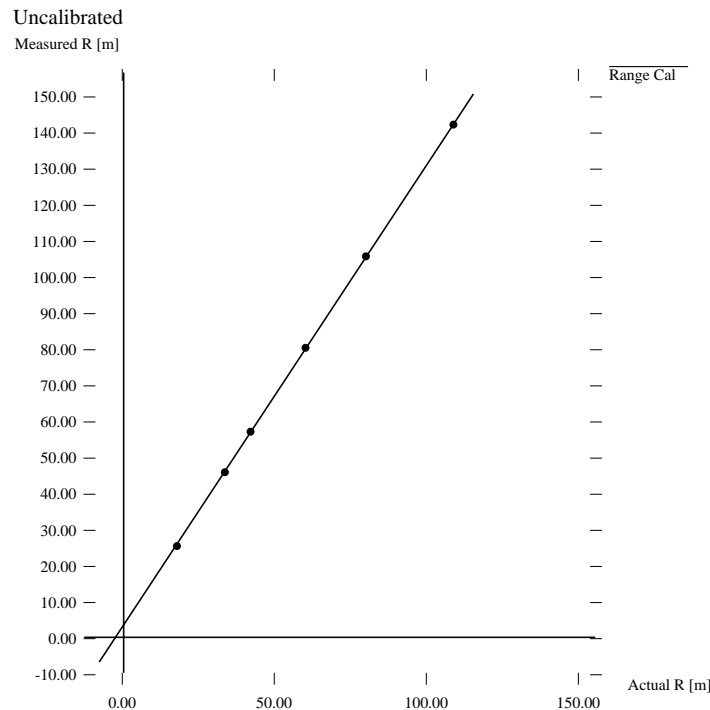


Figure 3.3 Range Calibration

We can now calculate the correct value of K , using the data points and the old value of K with which they were measured:

$$K = K_{old} \cdot \frac{R_{measured}}{R_{actual} + R_{off}} = 2.30 \quad [\text{kHz / m}] \quad (3.8)$$

It should be noted that this calibration procedure still contains some remaining errors as there is about a 10 cm error in measuring R_{actual} and an additional error due to target size. If necessary, these errors could, however, be reduced by a different setup.

3.2 Bearing Measurement and Calibration

Target bearing is obtained by using the phase information from adjacent receiver channels as described in section 2.3.2. The peak in the FFT across channels indicates the location of the target. The four input data points are zero padded to $N = 256$. Over a 12° field of view, the FFT output points are then given on a grid that is close to the theoretical achievable bearing accuracy of 0.047° (see section 2.2.2). Thus target bearing is calculated by,

$$\alpha = \arcsin \left[\left[i - 1 + \left(\frac{1-N}{2} \right) \right] \cdot \frac{\lambda}{\Delta x \cdot N} \right] \quad i = 1 \dots N \quad (3.9)$$

where Δx is the spacing between adjacent receivers and λ is the wavelength.

3.2.1 Phase Distortion

The obtainable accuracy of the bearing estimation depends largely on the amount of relative signal phase distortion between receiver channels. Therefore, great care was taken while designing the system to use only components with minimal or smooth phase distortion in each receiver channel path. This applied both to the millimeter wave front end as well as the digitizer of the radar. For this reason, a ten pole Butterworth filter was chosen as antialiasing low pass. This filter exhibits a smooth phase distortion and quick roll-off with a 60-dB stopband attenuation. Also, the phase distortion was matched by the manufacturer for the four filters in the receiver channels to minimize relative distortion and keep it constant over a large frequency bandwidth (Figure 2.4). The system also provides a calibration signal input that can be used to measure relative phase distortion between channels for different IF frequencies (see Figure 2.4).

To determine and correct relative phase distortion at a particular frequency, we used the following procedures:

The FFT output from the digitized time signal for each channel results in a complex number at each frequency data point. Magnitude A and phase φ at each point can then be expressed by the following relations (Figure 3.4):

$$A = \sqrt{Re^2 + Im^2} \quad \varphi = \text{atan} \frac{Im}{Re} \quad (3.10)$$

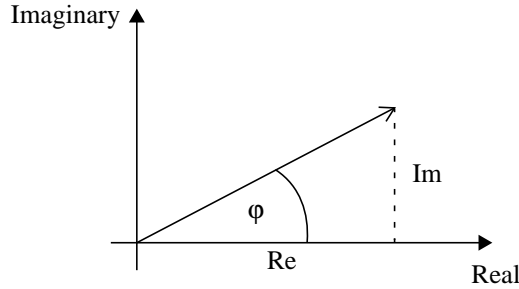


Figure 3.4 Complex FFT output

$$\begin{aligned} A_1^2 &= Re_1^2 + Im_1^2 \\ \varphi_i &= \text{atan} \frac{Im_i}{Re_i} - \Delta\varphi_i \quad i = 2 \dots 4 \\ Re_i^{new} &= \sqrt{\frac{A_1^2}{1 + (\tan\varphi_i)^2}} \quad -90^\circ \leq \varphi \leq 90^\circ \\ Re_i^{new} &= -\sqrt{\frac{A_1^2}{1 + (\tan\varphi_i)^2}} \quad -90^\circ > \varphi > 90^\circ \\ Im_i^{new} &= Re_i^{new} \cdot \tan\varphi_i \end{aligned} \quad (3.11)$$

Note that ϕ is an arbitrary absolute phase but does indicate the correct relative phase between channels. The relative phase distortion with respect to channel 1 is then determined by placing a point reflector in front of the sensor at bearing $\alpha = 0^\circ$ and computing,

$$\Delta\phi_i = \text{atan } \phi_i - \text{atan } \phi_1 \quad i = 1 \dots 4 \quad \Delta\phi_i \in [-180, 180] \quad (3.12)$$

$\alpha = 0^\circ$ is defined by the user as the direction as closely aligned to the optical axis of the sensor as possible.

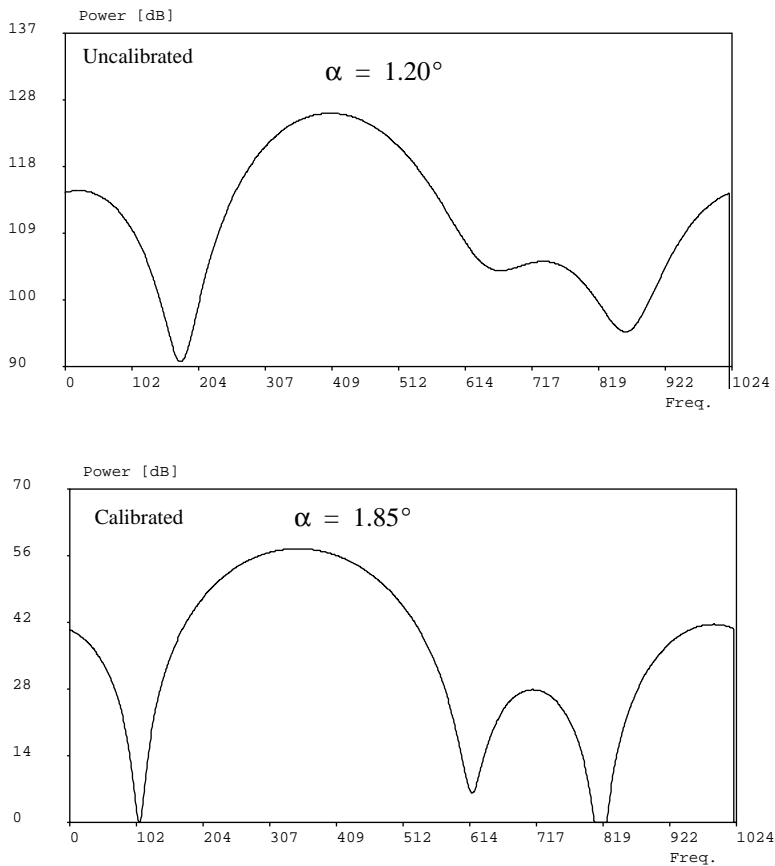


Figure 3.5 Phase Correction

Ideally, if there is no phase distortion, $\Delta\phi_1 = \Delta\phi_2 = \Delta\phi_3 = \Delta\phi_4 = 0$. However, this is usually not the case and we use the data set of $\Delta\phi_i$ to calibrate and correct each measurement. In order to avoid errors, we also need to normalize the signal amplitude in each channel, because channels may have different gains. Thus, phase corrections for channels 2 to 4 are carried out as shown in equation (3.11).

Figure 3.5 shows the FFT output for computing target bearing before and after the phase correction was applied. Since absolute signal amplitude values do not carry much significance, the amplitude values shown in Figure 3.5 for the ‘Uncalibrated’ and ‘Calibrated’ case were not normalized and are therefore different. In the ideal case, i.e. no phase distortion, we would expect the ‘Calibrated’ result to show one mainlobe and two sidelobes for a single target (see CHAPTER 2, Figure 2.8(c)). Since target range is proportional to frequency in an FMCW radar system and phase distortion may not be uniform over the entire frequency range, a table for different frequencies may need to be calibrated. However, in the case of this radar system there were negligible differences in phase distortion for target ranges between 4 and 100 meters.

We can observe in Figure 3.5 that, in the ‘Calibrated’ case, even though the mainlobe appears broader, it is better defined and there is less leakage into the adjacent right sidelobe than in the ‘Uncalibrated’ case. The other sidelobe on the far right contains slightly more signal power than the first one. This indicates the possible presence of a second reflector in this particular range/bearing cell. In fact, the target in this case was a person standing at a range of 15 meters in front of the sensor. Hence, the sensor did not look at a point target, but rather at one with multiple reflectors. (Refer also to section 2.3.2).

3.3 FFT Data Windowing and Target Detection

As explained previously in section 3.1 , significant leakage effects can be encountered in the frequency spectrum output of the FFT. This is a result of the fact that the data sampling interval has to be of finite length and thus, in effect, the data set is convolved with a rectangular window function (refer to [8] and [24]). Leakage effects cause signal power to be present in sidelobes adjacent to the mainlobe of a target. Sidelobes usually taper off for an infinite distance away from the target. If several targets are in close vicinity, the resulting signal powers are superimposed and under certain conditions could raise the sidelobe level above the target detection threshold. Several methods are available to alleviate this problem, among them

numerous CFAR (constant false alarm rate) algorithms as described in [4] and [19] and different window functions to reduce sidelobe levels (refer to [8], [21] and [24]).

Usually any window function that tapers off towards the ends will suppress the sidelobes to a greater or lesser extent. Unfortunately, this effect has to be traded off with an increase in the width of the mainlobe. Depending upon the application and the desired sidelobe characteristics, different window functions can be selected. Some popular windows are Parzen (triangular), Hanning, Hamming and the Kaiser window. For a detailed discussion of different window functions and their trade-offs, the reader is referred to the literature (see [8]).

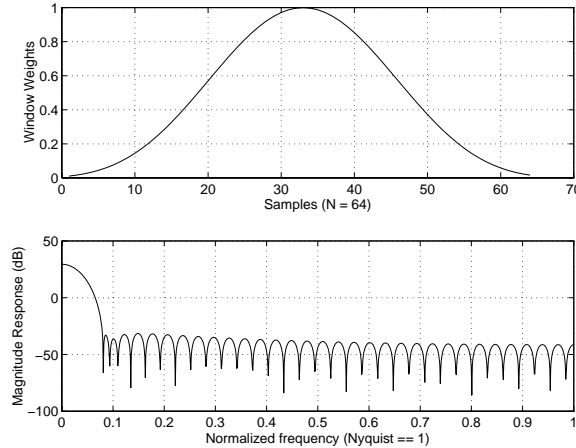


Figure 3.6 Time domain signal and DTFT of window function

In the case of this radar system, the sensor is potentially used in a variety of different conditions. The environment could be fairly cluttered. Also, strong reflectors could be very close to weak reflectors. Under these conditions, we were interested in a window function that would keep the mainlobe as narrow as possible. In addition, the sidelobes should be well attenuated and exhibit predictable characteristics. An appealing window function under these aspects is the *Dolph-Chebychev* window. It has a reasonably narrow mainlobe with a uniform sidelobe level [8]. We selected a variant of this window function that is mathematically easier to implement and which is discussed in reference [29]. The general, continuous and parametric form of the window can be expressed as follows:

Calibration and Target Detection

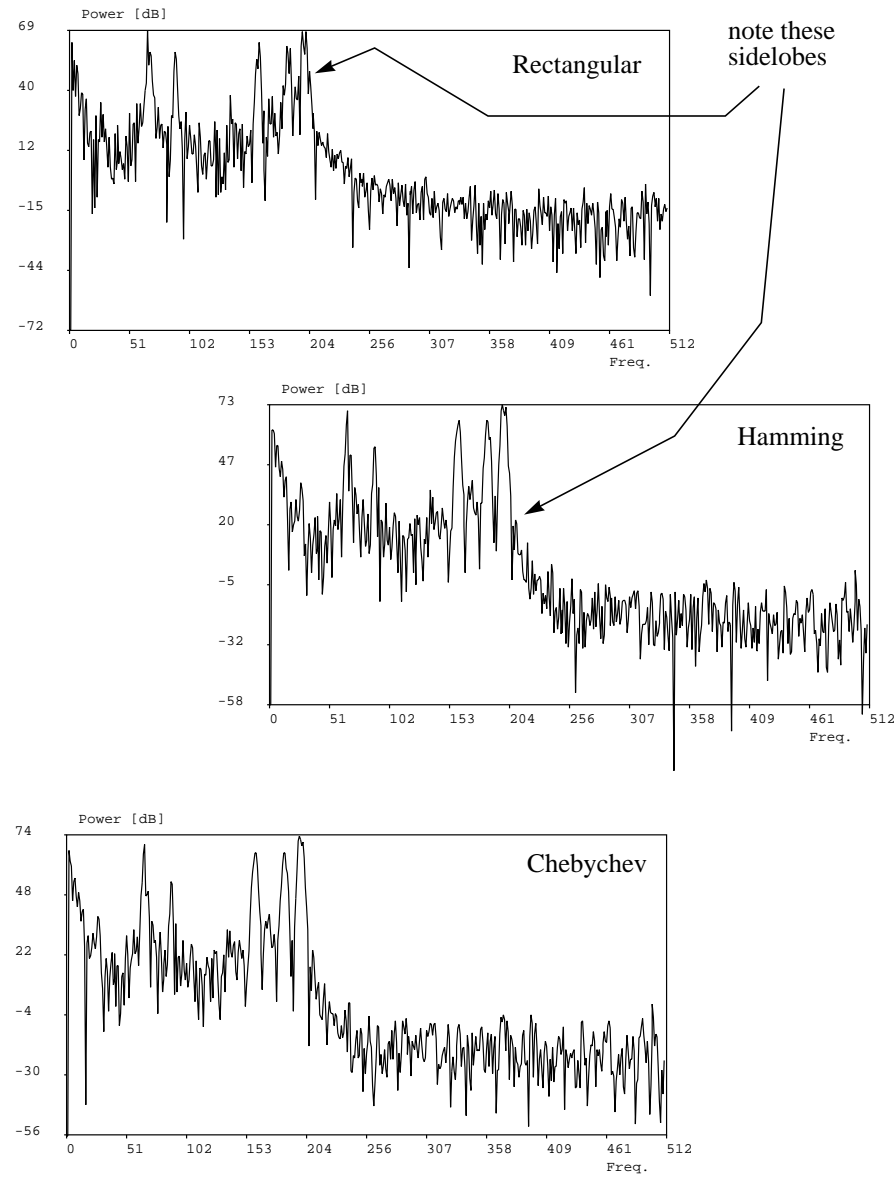


Figure 3.7 FFT output using same input data set, but different windows

$$w(t) = \left[1 - a \left(\tanh b \pi \frac{t}{T_m} \right)^p \right]^r \quad (3.13)$$

where $\pm T_m$ is the width of the window; a, b are the window parameters and are real numbers; p, r are the exponents of the window and are natural numbers.

Figure 3.6 shows the corresponding time domain signal and power spectral density function of equation (3.13).

The effect of different window functions on a data set of $N = 1024$ is shown in Figure 3.7. In this case no background noise removal (section 3.1.1) was performed. Note that the corner frequency of the antialiasing filter is at $i = 256$ on the frequency axis. The data set corresponds to the traffic scene shown in Figure 3.12. As predicted, we can observe that the rectangular window has the worst sidelobe fall-off. The other two windows have a much better separation between target peaks and noise level. Note that the signal power axis is logarithmic. The Hamming and Chebychev window functions have a very similar performance. The Chebychev window (equation (3.13)) gives a slightly better target separation from the sidelobes and a higher target intensity. Also, it generates a uniform, constant sidelobe level which simplifies the succeeding target detection task.

Window functions are only used for obtaining the power spectral density functions for range estimation. No window function, i.e. a rectangular window, is used to obtain the power spectral density function for bearing estimation. In the latter case, it is more important to have narrow mainlobes, rather than attenuated sidelobes, so that multiple targets can be detected within the given resolution limits.

Valid targets are then detected by finding all peaks above a uniform threshold, starting with the strongest target. The actual threshold level is determined by calculating an approximate noise level and adding a constant value which is determined empirically. A value for the noise level is computed by finding the maximum power within a range of $i = 256 \dots 1024$. This is outside of the range where a target could appear and signal power appearing in this interval is mostly due to sidelobe effects and noise.

In the case of an extended target as shown in Figure 3.8, multiple reflectors are detected on the same physical object. Because of multipath effects and small object and sensor movements, the detected locations can jump considerably in range. For this reason, if adjacent target peaks are within a certain signal power range ΔP , only the maximum peak is reported. This target peak is assumed to be the most stable.

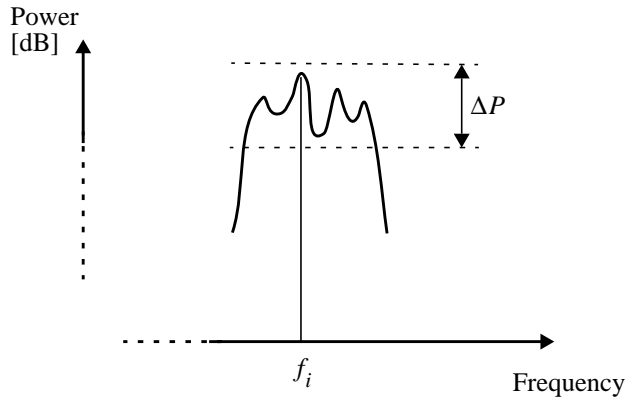


Figure 3.8 Extended Target

For each target detected in the range spectrum, we apply a second FFT as described in section 2.3.2 to determine the bearing of one or multiple targets present at this location. Following, we determine the maximum peak in the bearing spectrum. This is the main target. As described in section 2.3.2 and given by theory, the first sidelobe due to this target is attenuated by 11.5 dB. Hence, we then check whether any other targets are present by searching for additional peaks whose signal levels are above a 11.5 dB attenuation from the maximum. In order to account for noise, the actual threshold is raised by an empirically determined constant.

Note that, as discussed previously in CHAPTER 2 , each range resolution cell can contain only up to a maximum of four distinguishable targets at different bearings.

3.4 Radar Performance Results

3.4.1 Accuracy

Tests of the repeatability and related accuracy of a radar measurement were performed in an open area test site, using a corner reflector as single target with a radar cross-section of approximately 7 m^2 . Figure 3.9 and Figure 3.10 show the

Radar Performance Results

obtained results for range and bearing in the case of a stationary target. Table 3.1 shows the corresponding mean value and standard deviation computed for each data set.

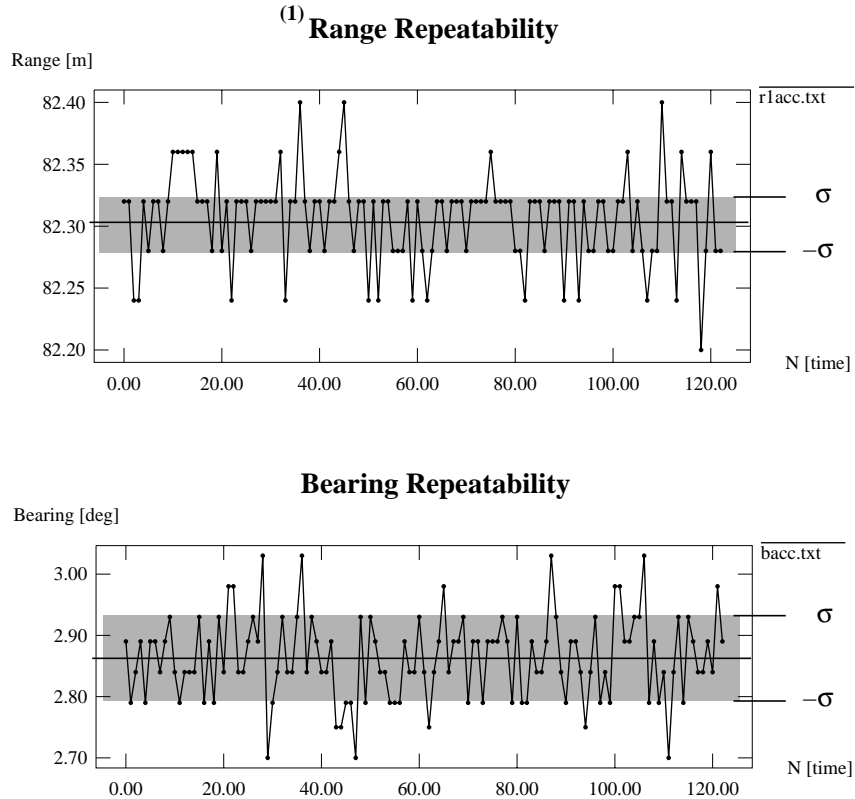


Figure 3.9 (1) Range and bearing repeatability and accuracy over time

The standard deviation σ is shown shaded in the data sets in Figure 3.9 and Figure 3.10. The data set (1)Range in Figure 3.9 has been calculated by using a 1024 point FFT and the approximation procedure explained in section 3.1 . The data set (2)Range in Figure 3.10 has been computed by using a 131,072-point zero padded FFT in order to try to obtain higher accuracy (refer to section 3.1). Here we used only $n = 40$ readings since the processing had to be done off-line.

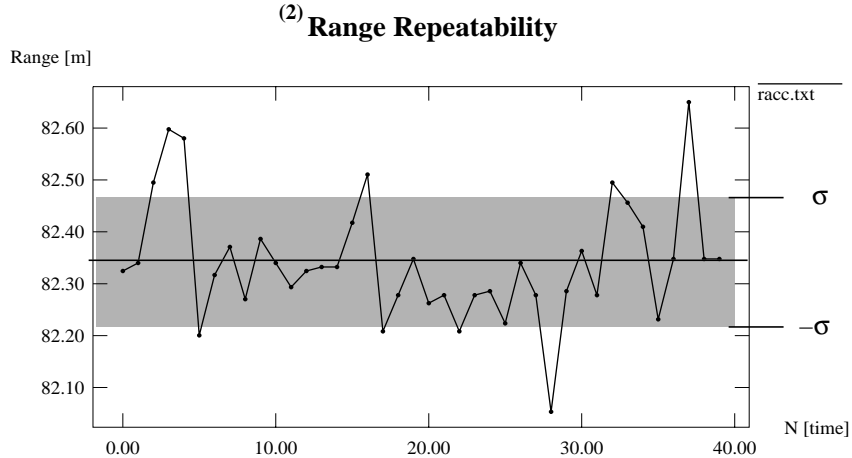


Figure 3.10 (2)Range repeatability and accuracy over time

	Bearing [deg]	(1)Range [m]	(2)Range [m]
number of samples n	123	123	40
mean \bar{x}	2.86	82.31	82.34
standard deviation σ	0.0685	0.0364	0.1161

Table 3.1 Statistics on Range and Bearing measurements

The values of the data sets in Figure 3.9 change in discrete steps, since the C40 DSP transmits numbers only up to the second digit after the decimal point, via the serial line connection to the host computer (see Figure 2.4). Currently, only a low speed serial link is available, limiting the total number of bytes that can be transferred in a reasonable amount of time. However, an upgrade to a high speed parallel link is straightforward and could be easily implemented.

For Figure 3.10 , the processing was done off-line using all available digits in floating point.

We can observe that the error values obtained for measuring target bearing, roughly correspond to the theoretically estimated values. The bearing errors are

probably largely due to phase noise in the mixers, amplifiers and filters. For the method used in computing range in data set ⁽¹⁾Range we expected about a 10 times improvement in accuracy over the 1 meter range bin given by a 1024 point FFT. This is more or less confirmed by the obtained error value shown in Table 3.1 .

We can observe that the error obtained for data set ⁽²⁾Range is the same order of magnitude as for data set ⁽¹⁾Range, but overall slightly larger. Theoretically, one would have expected much smaller errors in this case (see section 2.2.2). However, due to zero padding, adjacent points are now likely to be correlated. Also, we suspect some possible numerical errors in the 131072 point FFT computation because we found that the maximum peak is in reality almost a plateau that changes only very little for a large number of adjacent points. In general, likely causes of range errors between consecutive range measurements are slope changes and nonlinearities in the FM sweep between successive sweeps.

Thus Table 3.1 also shows that the parabola approximation of an FFT peak as discussed in section 3.1 , is a valid method for improving range accuracy.

The resolution abilities of the radar system in range were tested by slowly moving two corner reflectors apart at a distance of approximately 35 meters. They could be detected as two distinct targets when the separation between them was larger than 0.93 meters ($N = 2048$). This is slightly larger than the expected 0.6 meters, but is probably due to the fact that both targets were mounted on a tripod and had a certain geometric extent. Also, the actual frequency sweep of the system is closer to 240 MHz than the originally planned 300 MHz.

Similarly, the resolution between two distinct targets in bearing was determined to be 3° , which is as expected by theory.

Finally, using a variety of real world targets, we found that the radar was able to detect people up to 50 m, cars up to 180 m and trucks up to more than 200 m.

3.4.2 Typical Traffic Scenarios

When testing the sensor system in a real environment, it performed well under a variety of operating conditions in the Pittsburgh area and Denver, Colorado. No deterioration of performance could be detected when operating in heavy rainfall and poor visibility conditions. Warm temperatures also did not seem to pose any problems. However, the sensor system did fail once after about 45 minutes when operating in temperatures around -20° Celsius. This was most likely due to the Gunn oscillator. These devices generally do not work well in very low temperatures. The problem could, however, be easily fixed by adding a heat element close to the oscillator.

Calibration and Target Detection

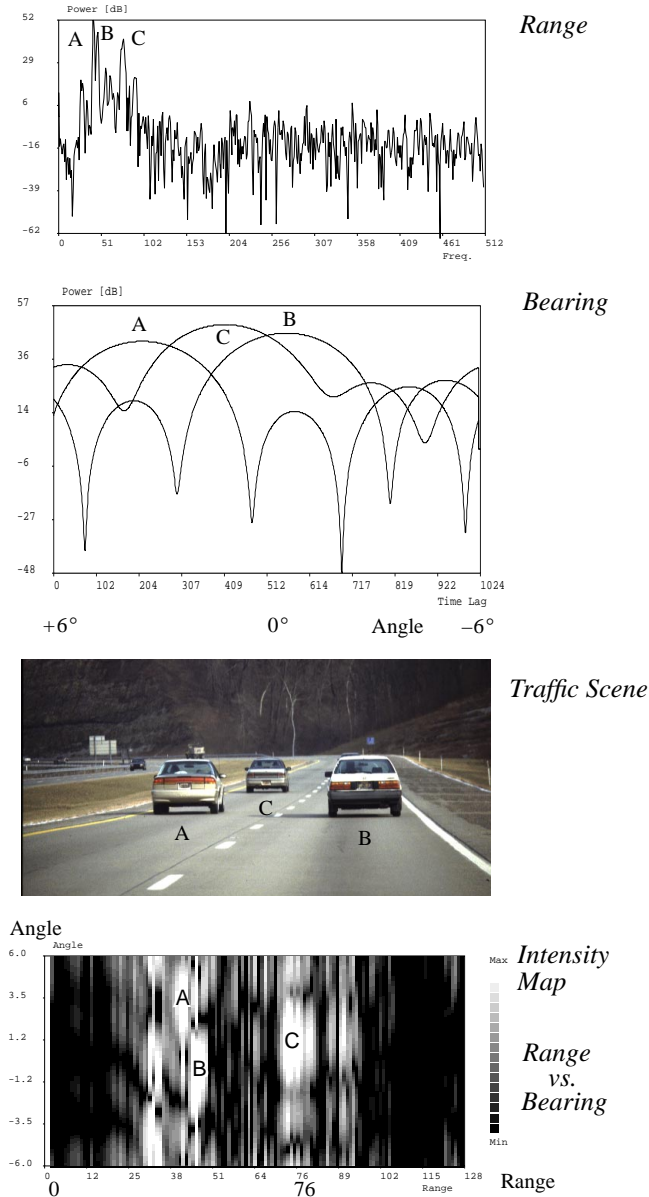


Figure 3.11 Radar Data for Scene 1 on Highway

Radar Performance Results

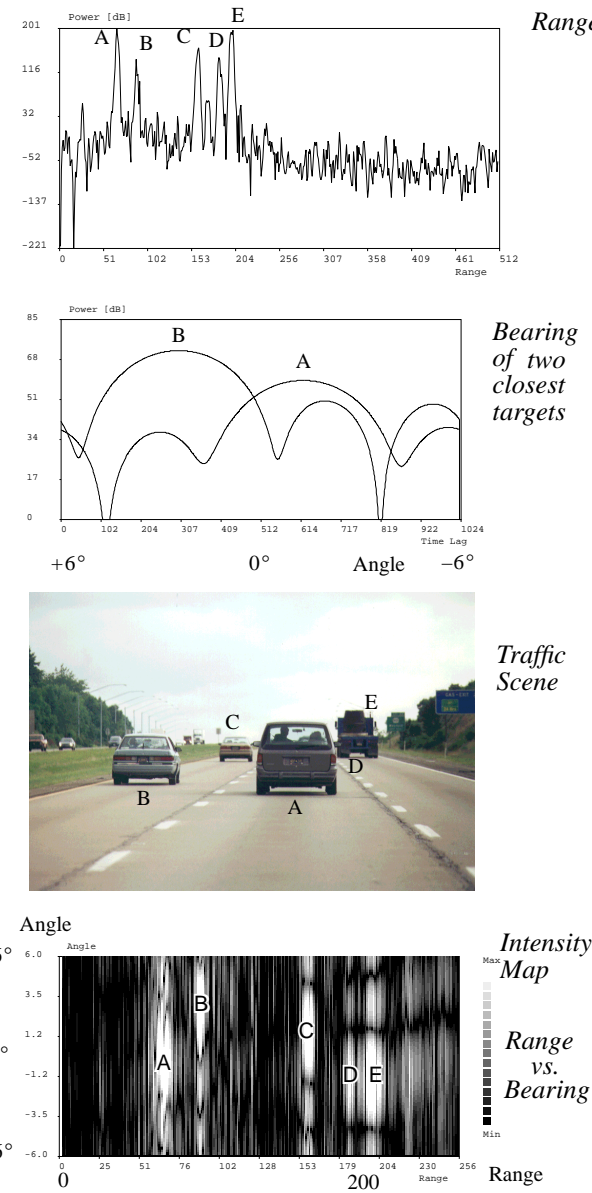


Figure 3.12 Radar Data for Scene 2 on Highway

Figure 3.11 and Figure 3.12 show plots of range, bearing and the corresponding scene picture of real data obtained with the sensor on a highway (I-279 north and I-79 north before the Wexford exit). Note that the bearing data appears quite smooth because only 4 data points are available. The remaining points are zero padded.

In both figures, the horizontal width of the picture showing the traffic scene corresponds approximately to the $\text{HFoV} = 12^\circ$ of the radar sensor.

3.5 Ghost Targets

Reflections from an object that do not appear at the correct location in the radar image, but instead at a mirrored position, are generally termed ghost targets. They can appear owing to ambiguities present in the data used for determining range or bearing.

In this radar system, ghost targets in range do not appear because the transmitter power is weak compared to the unambiguous range of the FM sweep (section 2.2). Ghost targets in bearing appear because of ambiguity in the phase measurement. As briefly mentioned in section 2.2.1, that is the case in this radar system due to current antenna design. Target bearing is proportional to the phase angle between adjacent receivers. It is independent of signal frequency and FM sweep rate.

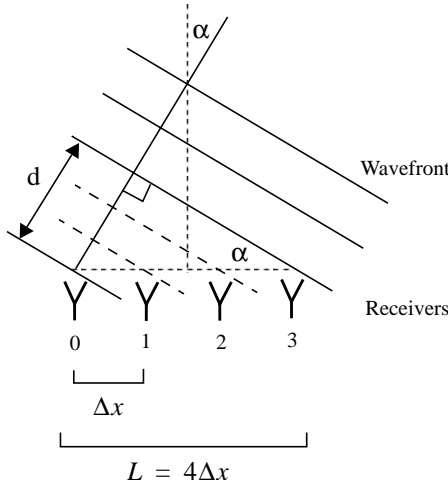


Figure 3.13 Receiver Geometry

Ghost Targets

The horizontal field of view (HFOV) of 12° corresponds to an unambiguous signal phase angle of 360° . For any target detected outside the HFOV, a phase wrap-around occurs and the target is mirrored back into the HFOV from the opposite side. Thus, a target detected, for example, at $+7^\circ$ will instead appear at -5° (see Figure 3.14). Due to an insufficient attenuation of the antenna sidelobes, this case occurs since a strong reflector can be detected in the sidelobe area.

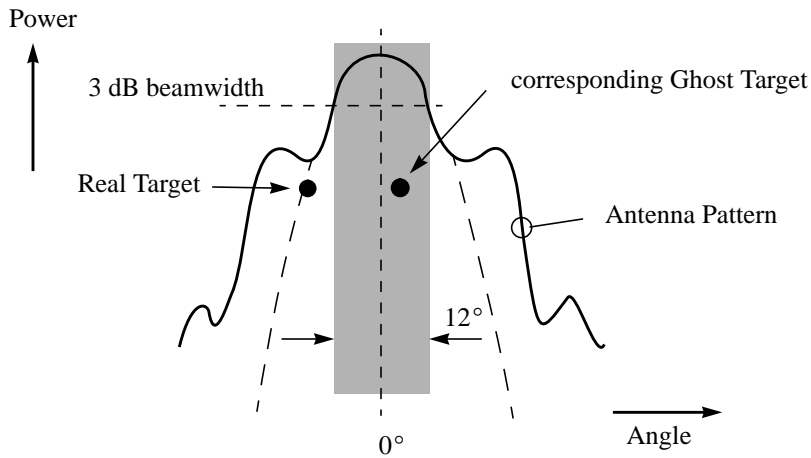


Figure 3.14 Ghost targets in bearing

In order to remove the ghost targets in bearing, we tried a method based on the idea of stereo vision. As shown in Figure 3.13, the time of flight for a wavefront reflected from a target off axis differs between receivers 0 and 3 corresponding to distance d . The angle α corresponds to target bearing. At the signal phase wrap-around conditions, we have,

$$d = 4\Delta x \cdot \sin \alpha \approx 7.8 \text{ [mm]} \quad (\alpha = 6^\circ) \quad (3.14)$$

with Δx calculated from equation (2.18). Note that for design reasons based on physics, the aperture of a single receiver element is approximately equal to the spacing Δx between receiver elements. Thus the aperture of the receiver array is $L = 4 \cdot \Delta x$.

Hence, in order to determine the actual direction of the incoming wavefront and reject ghost targets that appear on the wrong side, we need to be able to measure a

range difference of $d \geq 7.8$ mm. It follows, that the frequency grid for the FFT in range would need to be zero padded to 131072 points, to obtain approximately an increment of 0.6 cm per bin. Computationally, this turns out to be quite expensive. In simulation, using matlab (see CHAPTER 2 , section 2.3.1), we were able to show that the range difference d could be detected with FFT processing if the target was outside the 12° field of view. However, unfortunately, the theoretical achievable range accuracy of the current radar system $\delta R_{rms} = 112$ mm, as given by equation (2.12) . Therefore, the current SNR of the radar system makes it impossible to use the above approach reliably. These observations were confirmed by experiment (refer to Table 3.1).

Thus, at this point, ghost targets in bearing could only be reduced by a significant redesign of the antenna system. From a practical point of view, a sidelobe attenuation of -20 dB is certainly achievable. Alternatively, an additional receiver element could be used, spaced a significant distance apart from the other four receivers. This would increase the baseline and hence the minimum distance d required.

Knowing how hard it is to collect a fact, you understand why most people want to have some fun analyzing it.

----- Jesse L. Greenstein

The previous two chapters described an obstacle detection system using a millimeter wave radar sensor. In CHAPTER 4 , we now discuss integration of the obstacle detection sensor with two different types of road geometry sensors, in order to improve obstacle classification abilities of the entire system. Both road geometry sensing systems have been developed by other people in the Navlab group at Carnegie Mellon University (refer to [10], [22] and [23]).

4.1 Problem Situations

In certain road environments, a false alarm situation may arise. This is especially the case for multilane roads, undivided highways, curved roads and roads that are bordered by stationary objects such as guard rails, road signs or trees. It is therefore important to have some information about the road geometry environment in which the vehicle is driving. On a straight stretch of road, assignment of obstacles to particular lanes and areas off road and on road is simple. On undivided roads it is,

however, important to know whether an object in front of the vehicle is in the vehicle's own driving lane, in the lane for oncoming traffic or off road. If the road is curved, an additional difficulty is to determine whether an object is in a neighbouring lane on a multilane road, the oncoming traffic lane on a two-lane road or off road altogether. Typical traffic situations are shown in Figure 4.1.

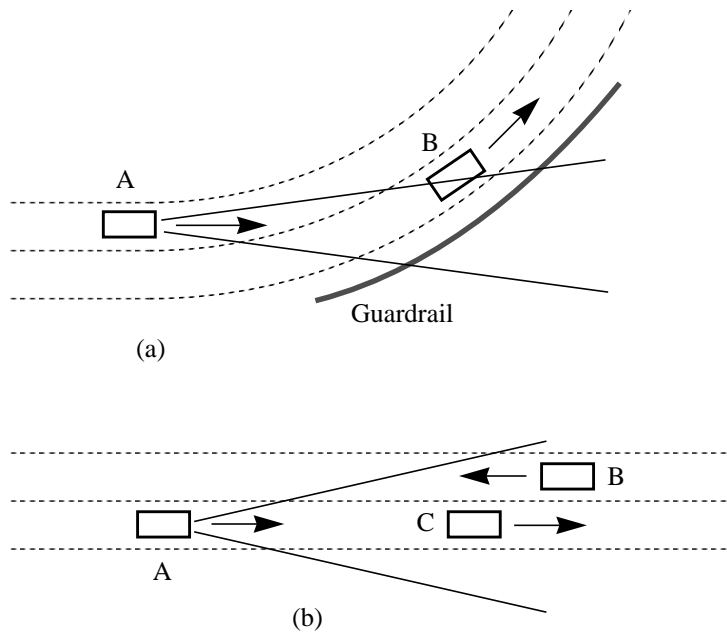


Figure 4.1 Traffic situations leading to potential false alarms

In Figure 4.1 (a), for example, vehicle A detects two targets ahead: vehicle B and a portion of the guardrail. It is obvious that neither object poses a threat if vehicle A stays in its current driving lane. However, a radar-only based sensor system will not be able to assess this situation properly without additional information about road geometry.

As a first step, information about steering radius from a steering encoder can be integrated. This will help to reject clutter and improve performance when the vehicle is driving through a bend. However, since in this case we only know the current vehicle state but cannot look ahead, the traffic situation in Figure 4.1 (a) still poses a problem. Here, the vehicle is still on a straight stretch of road and does not know yet

of the curve ahead. Similarly, in Figure 4.1 (b) for a two-lane road, we need to know that vehicle C is in our driving lane, and whether the approaching vehicle B is in the oncoming traffic lane or using our driving lane for an overtaking manoeuvre.

In the following subsections, we will discuss a more detailed analysis of these road geometries.

4.1.1 Geometric Analysis of different traffic scenarios

From the traffic scenario shown in Figure 4.1 (a) and Figure 4.2, we want to determine the radius of the curve that would place a vehicle B in the driving lane instead of the adjacent lane. We assume that the curve starts at $L = 19$ meters ahead of vehicle A, where the sensor's field of view (FoV) just covers an entire lane. Also, the average lane width is assumed to be 4 meters.

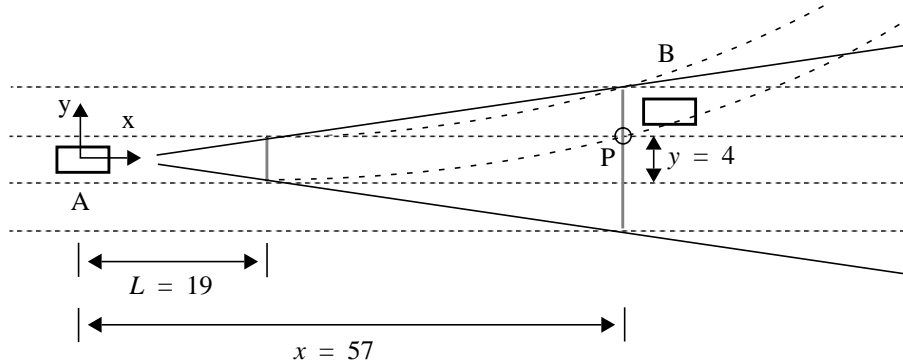


Figure 4.2 Road Curvatures and Sensor FoV

If we place the center of the curve at (r, L) and use the equation of a circle through point P, then the radius r of the curve is given by,

$$r = \frac{(x - L)^2 + y^2}{2(x - L)} = 182.5 \text{ m} \quad (3.15)$$

This road curve radius lies well within the range typically encountered on a rural road. On multilane highways, road curvatures are usually less, which makes it likely that the above ambiguous situation will be encountered.

Figure 4.1 (b) shows a traffic scenario typically encountered on a two-lane road. Here, the range sensor must be able to distinguish vehicles in different lanes. Suppose that vehicles B and C are at 100 m distance from vehicle A and, again, we assume the lane width to be 4 m. Then, in order to resolve vehicles B and C as two point targets, we must be able to resolve an angular bearing of $\text{atan}(4/100) = 2.3^\circ$. Similarly at 57 meters, the target separation for vehicles in adjacent lanes would be 4.0° , and at 200 meters it would be 1.15° .

4.1.2 Minimum turn radius that keeps vehicle within FoV of sensor

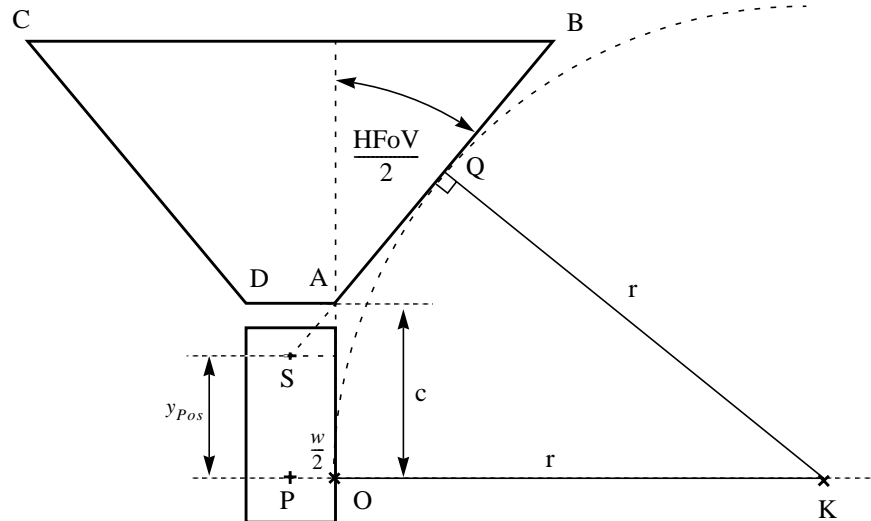


Figure 4.3 Minimum Turn Radius

When driving on curved roads, it is also important to know the road curvature limit beyond which the radar sensor cannot illuminate the entire road area while driving around a bend. However, it should be noted here that, since wave propagation is line of sight, a radar sensor can never look around a bend unless there are reflectors in between.

The sensor is assumed to be mounted at location S on the vehicle. The minimum

Problem Situations

turning radius r_{min} is then given by the following equations, where y_{Pos} is the offset between sensor origin S and vehicle origin P, w is the vehicle width and HFoV is the horizontal field of view. The equation of the boundary line of the sensor field of view is given as $y = mx + c$. For simpler calculations, the origin is taken at point O:

$$m = \cot\left(\frac{\text{HFOV}}{2}\right) \quad (4.1)$$

$$c = y_{Pos} + \frac{w}{2} \cot\left(\frac{\text{HFOV}}{2}\right) \quad (4.2)$$

As shown in Figure 4.3, the rear wheel at point O tracks the boundary of the area swept by the sensor's field of view when turning with r_{min} . The boundary line AB is tangent to the arc OQ at Q and their equations are given by,

$$y = mx + c \quad \text{and} \quad (x - r)^2 + y^2 = r^2 \quad (4.3)$$

Thus, the discriminant $B^2 - 4AC = 0$ for the resulting quadratic equation in x , when substituting y , and we obtain finally,

$$r = mc + c\sqrt{m^2 + 1} \quad \Rightarrow \quad r_{min} = \frac{w}{2} + r \quad (4.4)$$

With the dimensions of the Navlab 5 test vehicle and $\text{HFOV} = 12^\circ$, we get,

$$r_{min} \approx 189 \text{ m} \quad \text{using} \quad w = 1.8 \text{ m} \quad y_{Pos} = 1.3 \text{ m} \quad (4.5)$$

4.1.3 Maximum road gradient



Figure 4.4 Road gradient

Another problem for sensor measurements when driving in an outdoor environment is the non-flat road surface. The sensor vertical field of view is limited to 3° to avoid unwanted reflections from overhead structures such as bridges or road signs and ground returns from close range. However, this also limits the maximum viewable range if we encounter a significant road gradient.

Thus, if the vertical field of view of the sensor $\text{VFoV} = 3^\circ$ and the sensor is mounted at a height $z_{Pos} = 1 \text{ m}$ above the ground, then the maximum gradient of the road that would still allow the sensor to see a target at $R = 200 \text{ m}$ is given by,

$$h = z_{Pos} + R \cdot \tan \frac{\text{VFoV}}{2} = 6.2 \quad (4.6)$$

This means that the equivalent instantaneous delta gradient would be about $h/200 = 3.1\%$. The corresponding vertical road curvature, which is a design parameter used by road builders, is given by,

$$c_v = \frac{2h}{h^2 + R^2} = 0.00031 \text{ [m}^{-1}] \quad (4.7)$$

Therefore, unless we drive in a mountainous region, the road gradient will have very little effect on the maximum viewable distance.

The above discussions have shown that it is important to have knowledge about road geometry, in addition to range information to potential obstacles. Unless road geometry is taken into account, a correct classification of objects is not possible in many traffic situations with respect to their influence on collision avoidance and navigational decisions. In the following sections, we will describe two approaches for integrating additional road information.

4.2 Object Classification and Local Map

Detected targets are kept in an object list (or local map) which is updated by successive data frames from the radar sensor (refer also to [18]). Each object has the following set of parameters or annotations associated with it:

$$\{Position(x,y), Amplitude, History, Decay, Lane\}$$

Position indicates the x-y position of the object with respect to the vehicle center.

Amplitude is the target strength.

History counts the number of times this particular object has been detected and tracked in successive frames.

Decay indicates when an object will be deleted from the list if it has not been seen for a successive number of frames.

Lane indicates the specific road lane or off-road location of an object with respect to the vehicle's driving lane.

Objects are tracked through successive frames within a specific window area and by using information about vehicle position changes. The size of the tracking window depends on the expected relative maximum speeds between objects and the frame update rate of the sensor.

In order to assess the danger an object poses to the vehicle's motion, we need to know the location of an object with respect to the vehicle's driving lane. This is a simple problem on a straight stretch of road, using only radar sensor data. However, on curved roads in cluttered environments it cannot be solved without additional information about road geometry as discussed before (Figure 4.1).

This information is provided either by the RALPH vision-based lane tracking system described in section 4.3 or by a GPS and digital road-map based system described in section 4.4. For classification purposes, the road lane center of the vehicle's driving lane is given as a set of points $P_i(x_i, y_i)$ and the road curvature $1/r_i$ between P_i and P_{i-1} . The first point P_0 indicates the offset of the vehicle center from the lane center and thus has no curvature associated with it. Hence, the road lane can be represented as a set of straight line and circular arc segments as shown in equation (4.8) for segment i .

$$y = m_i \cdot x + c_i \quad \text{or} \quad (x - h_i)^2 + (y - k_i)^2 = r_i^2 \quad (4.8)$$

A straight line or circular arc is chosen, depending on the road curvature of that particular segment:

```
If  $r_i \geq 1000$ 
    use straight line segment
else
    use circular arc.
```

The points are spaced approximately 20 meters apart on average, but the spacing can be variable and is chosen depending on available look-ahead distance and shape of the road. Given equation (4.8) and assuming an average highway lane width of

Integration with Road Geometry System

4 meters, or using the lane width estimate given by the vision system (section 4.3) or road-map (section 4.4), we can now determine whether an object is inside or outside the current lane boundary and its distance to the boundary. The *Lane* parameter for each object in the list is then updated accordingly. Each increment or decrement in *Lane* is equivalent to a lane width displacement to the right or left of the current driving lane, where zero indicates the current driving lane. Thus, the values shown for *Lane* have the following meaning:

<i>Lane</i>	Object Location
.....	
-2	Object is in the second lane to the left or off road
-1	Object is in the left adjacent lane
0	Object is in the driving lane of the vehicle
1	Object is in the right adjacent lane
2	Object is in the second lane to the right or off road
.....	

In addition, another future map parameter could be *Velocity*, which would be the doppler velocity between the radar sensor and an object. However, currently it is not available since doppler velocity processing has not yet been implemented on the radar. As shown in CHAPTER 2, section 2.2, the maximum expected range error due to doppler velocity is about 5.7 meters. For moving objects, travelling in the same direction, this error will be less. For objects moving in the opposite direction (positive doppler velocity) the error will be larger, but it adds to the actual range value. Thus moving and stationary objects approaching the vehicle will appear at a larger range than they are in reality. Thus it is unlikely that an object located outside the driving lane of our test vehicle would erroneously be placed in the driving lane due to a range-doppler error. In a collision avoidance scenario, the range-doppler error would only have a negative impact if the object is detected relatively close to the radar sensor. If the object is detected further away, then the maximum range-doppler error is too small to be significant.

The information in the local obstacle map can then be used by the Navigator in order to take appropriate actions, depending on distance to closest obstacle in the vehicle's driving lane and obstacles in adjacent lanes (see Figure 4.5).

4.2.1 Integrated System

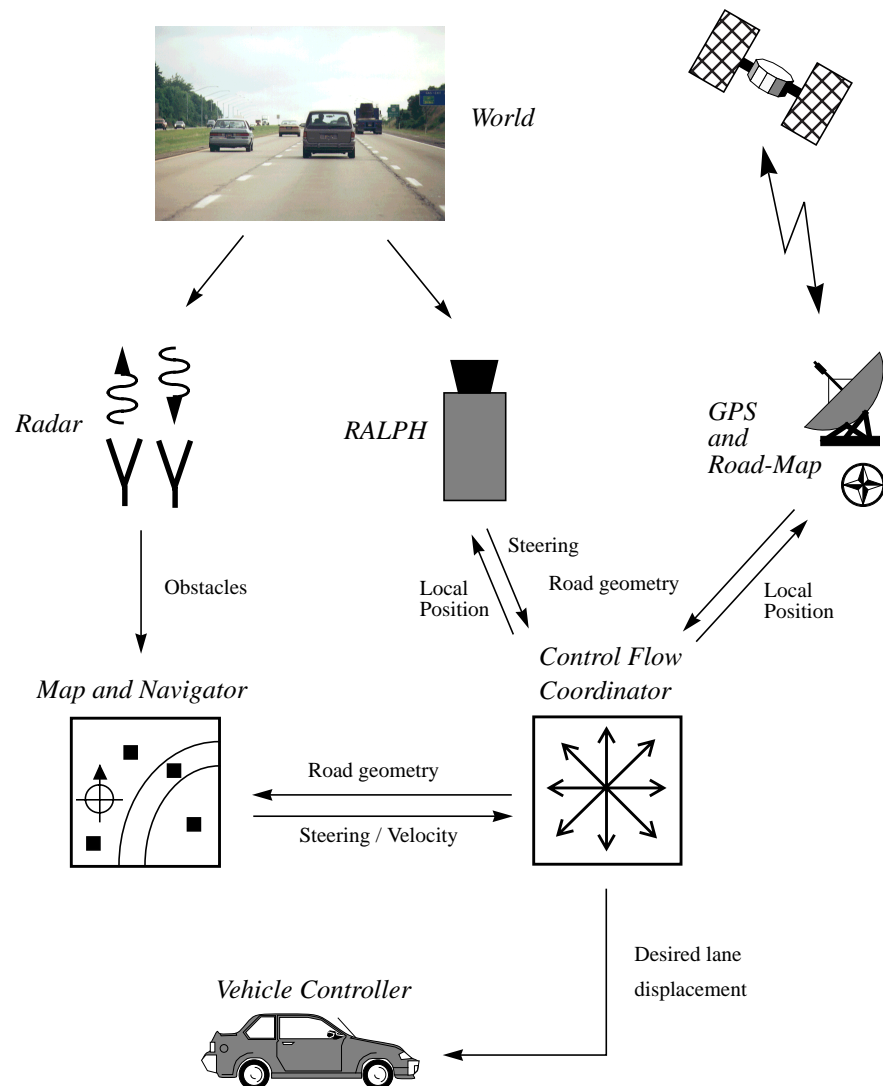


Figure 4.5 Data and control signal flow diagram for integrated system

Figure 4.5 shows the interconnections for the data and control signal flow in the integrated system. The radar is always used for detecting obstacle locations. Either the vision system (RALPH) or the GPS/road-map system are used for sensing road geometry. Currently, only one of the road geometry systems is used at a time. Both of these systems use local vehicle position information from odometry, as computed by the controller using wheel encoders and a yaw sensor.

When using the GPS/road-map system, the vehicle is steered manually and speed is controlled autonomously.

When using RALPH (see section 4.3), both the vehicle steering and speed are autonomously controlled. In this case, under normal driving conditions, the Control Flow Coordinator (CFC) takes RALPH's computed vehicle lateral displacement from the center of the lane and its estimated road curvature value, and passes them to the vehicle controller which then attempts to recenter the vehicle in the driving lane.

The radar sensor sends detected obstacles to the Map/Navigator module. Here, obstacles are tracked through successive frames in the local map and combined with the road geometry information for danger level classification. Overriding velocity commands are sent back to the CFC in order to maintain a safe driving distance to preceding vehicles. Also, steering arcs that need to be inhibited in order to avoid collisions with vehicles or objects present in adjacent lanes are sent to the CFC (refer to [18]).

4.2.2 Velocity setting through cruise control

The Navlab 5 test vehicle that has been used for most of this research does not have a fully functional vehicle velocity control. Speed control is available only through the built-in Cruise Control system. The Cruise Control, unfortunately, does not take velocity commands as input, but instead uses three states to control vehicle speed:

[*Decelerate, Maintain, Accelerate*]

Therefore, a simple algorithm was developed for changing vehicle speed depending on desired speed and the closest obstacle present in the vehicle's driving lane. For the following description, ΔR is the difference between actual range and desired safety range to a preceding vehicle, ΔV is the relative velocity between the two vehicles, and ε_R and ε_V are the allowable margins of error for ΔR and ΔV respectively before a state change is triggered.

```
If  $|\Delta V| < \varepsilon_V$  and  $|\Delta R| < \varepsilon_R$  (within velocity and range margins)
    set State → Maintain
else if  $\Delta V < 0$  and  $\Delta R > 0$  (object receding and object too far)
    set State → Accelerate
```

Results using Vision

```
else if  $\Delta V < 0$  and  $\Delta R < 0$  (object receding and object too close)
    set State → Maintain
else if  $\Delta V > 0$  and  $\Delta R > 0$  (object approaching and object too far)
    set State → Maintain
else if  $\Delta V > 0$  and  $\Delta R < 0$  (object approaching and object too close)
    set State → Decelerate
```

In addition,

```
If  $V > DesiredVelocity$  and State = Accelerate
    set State → Maintain
```

4.3 Results using Vision

RALPH (**Rapidly Adapting Lateral Position Handler**) is a vision-based adaptive system which can learn the current road features. It uses a weak model of road geometry and image reprojection to extract and adapt to the relevant features for driving. We used it here as an example of a vision-based approach for determining road geometry.

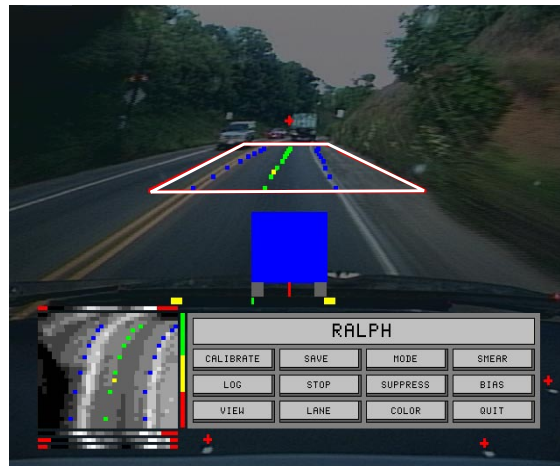


Figure 4.6 RALPH display for typical highway scene

Integration with Road Geometry System

In order to locate the road ahead, RALPH first resamples a trapezoid-shaped area in the video image, much like a birds-eye virtual camera, to eliminate the effect of perspective (Figure 4.6). RALPH then uses a template-based matching technique to find parallel image features in this perspective-free image. These features can be as distinct as lane markings, or as subtle as the diffuse oil spots down the center of the lane left by previous vehicles. RALPH rapidly adapts to varying road appearance and changing environmental conditions by altering the features it utilizes to find the road. This rapid adaptation is accomplished in less than one second, without human intervention [23].

Since RALPH can exploit any visible features running parallel to the lane, instead of relying exclusively on the presence of distinct lane markings, it can operate in a wider variety of situations than previous road following systems. In one experiment, called “No Hands Across America”, RALPH steered the Carnegie Mellon Navlab 5 test bed vehicle 98% of the 2850 mile journey from Washington, DC to San Diego, CA [23]. During the trip, RALPH drove at an average speed of 100 km/h (65 m.p.h.), in conditions which included bright sunlight, dusk, rain and night time. During one stretch in Kansas, RALPH drove continuously for 110 km (69 miles) without the safety driver touching the steering wheel.

Condition	Mean Error [cm]	Error [cm], Standard Deviation
Daytime highway	11.4	14.3
Daytime highway with shadows	13.8	18.9
Nighttime highway	11.1	13.8
Daytime rural road	13.7	16.2
Daytime rural road with glare	15.8	17.2
Nighttime rural road	13.8	16.8
Average	13.2	16.2

Table 4.2 Accuracy of Ralph’s lane-location estimation [23]

Typically, RALPH processes a road image within a trapezoidal area bounded longitudinally at about 20 and 70 meters ahead of the vehicle (Figure 4.6). It then combines its estimate of the vehicle’s lateral offset and the curvature of the road ahead into an estimate of the lane-center location about 30 meters ahead of the vehicle (approximately 1 second look-ahead at 100 km/h). Table 4.2 shows typical accuracies

Results using Vision

obtained with RALPH in estimating the road curvature ahead under a variety of driving conditions. The data is taken from experiments discussed in [23]. We observe that, on average, the error on rural roads increases slightly. RALPH assumes a flat ground plane for its image projection, and the increase in error is most likely due to a change in camera perspective due to hills in the area where experiments were conducted.

Overall, the error in lane-center and, hence, road geometry estimation from RALPH is less than 20 cm, even under the worst driving conditions. At a range of 100 meters, in practice, the radar sensor can locate the lateral offset of an object approximately within

$$\varepsilon_{lat} = 100 \cdot \tan 0.1^\circ \approx 17.5 \text{ [cm]} \quad (4.9)$$

(Refer to 3.4.1). Thus, given the measurement accuracies of the radar sensor and the lateral extent of expected roadway obstacles, we can see that a road lane classification of detected obstacles can be performed without any problems. Vehicles will generally drive close to the center of a lane, unless they are in the process of changing lanes. Assuming an average lane width of four meters, we can see that an object will always be placed correctly in its lane, given the total amount of measurement errors from above. This result has been confirmed by experiment: overall, we drove manually and autonomously for more than 150 km on highways during separate experiments, using the integrated sensor system in a combination of the radar sensor and RALPH.

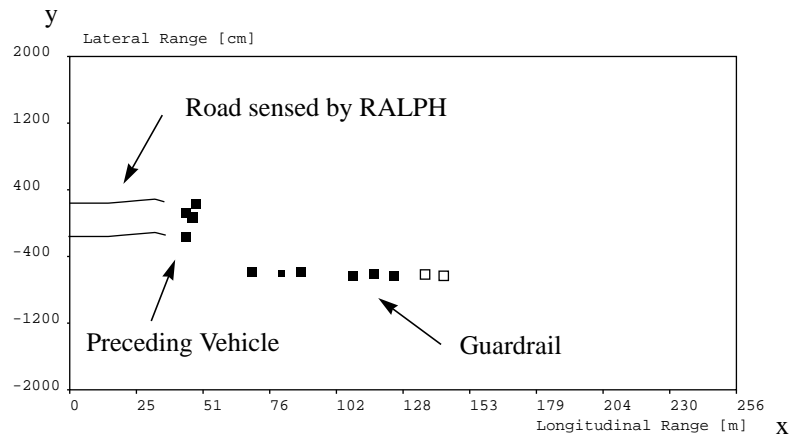


Figure 4.7 Integrated radar obstacle and vision road-map

Figure 4.7 shows a typical traffic scene as seen in the combined obstacle and road-map.

RALPH's usual look-ahead distance ranges between 25 and 60 meters. It is adjusted, depending partly on vehicle speed. Also, other vehicles travelling ahead may obscure part of the road in the image, thereby reducing the available look-ahead distance. Therefore, even though the radar sensor can detect multiple vehicles up to a range of more than 200 meters, the effective range for object localization and classification is limited by the momentary look-ahead distance of RALPH. In practice, this is not as much of a problem as the limiting factor is usually another vehicle in the driving lane, and vehicle speed is adjusted according to the separation distance and closing velocity which are measured by the radar.

Figure 4.8 (b) shows distance to a preceding vehicle tracked in the test vehicle's driving lane over time. Figure 4.8 (a) shows the corresponding vehicle path, augmented with approximate locations of some static features near the road. Here, the radar is able to detect the guardrail and eliminate it correctly. The bridge is not detected.

Similarly, Figure 4.9 shows distance to a preceding vehicle tracked in the test vehicle's driving lane over time. Figure 4.9 (c) shows the result obtained when using the road geometry information given by RALPH. Figure 4.9 (a) shows the corresponding vehicle path. Figure 4.9 (b) shows the result with the same radar data, but without using road geometry data, i.e. the road lane is assumed to be straight all the time. We can observe, as indicated in the figure, that the performance of the integrated system is much better on curved road segments. When tracking a preceding vehicle, road geometry data from RALPH is, at most, available only up to that vehicle, since RALPH's view of the road further ahead is obscured. Therefore, in order to always ensure a correct lane classification of the preceding vehicle, we extrapolate the road for approximately 30 meters past the last road point given by RALPH. For the extrapolation, we use the average road curvature given by the last road segment frame from RALPH. Since, from experiment, the last road point given by RALPH tends to be noisy, it is not used for the extrapolation calculations. As road shape usually does not change much over a distance of 30 meters, we found a tangential linear road extrapolation to be sufficient in practice. The size of the target tracking window was 10×10 meters, and we always recorded the closest detected object in the driving lane. Both RALPH and the radar sensor are calibrated with respect to the vehicle origin. Hence, road points and object points are given in vehicle-centered coordinates and thus merged. With radar data updates being provided at 3 Hz and road geometry updates available at 15 Hz, matching errors due to time delays were not significant. Uncertainty of object and road location, increases with distance from the vehicle due to measurement errors and a possible yaw offset error between radar and road geometry sensor. Therefore, for each frame, all

Results using Vision

obstacles are reclassified with respect to the currently available road geometry data. All previous lane classification is discarded. Thus, errors are avoided in the event an object approaching the vehicle is incorrectly classified at long range.

Figure 4.10 shows the same results as Figure 4.9 on a different road segment. We can observe, both in Figure 4.9 and Figure 4.10, that the range to the tracked car sometimes jumps by a few meters. This most likely occurs because the radar views the vehicle under a slightly different aspect angle, and another reflector closer to the front of the car becomes more prominent.

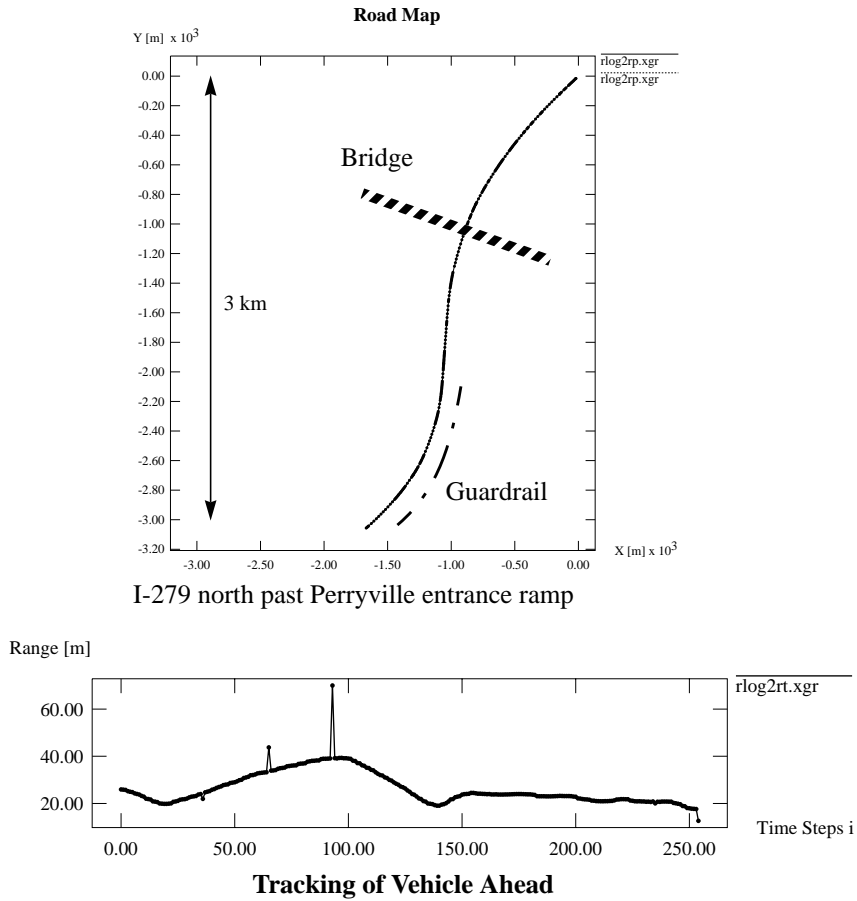


Figure 4.8 Tracking vehicle ahead in driving lane (Radar & Vision)

Integration with Road Geometry System

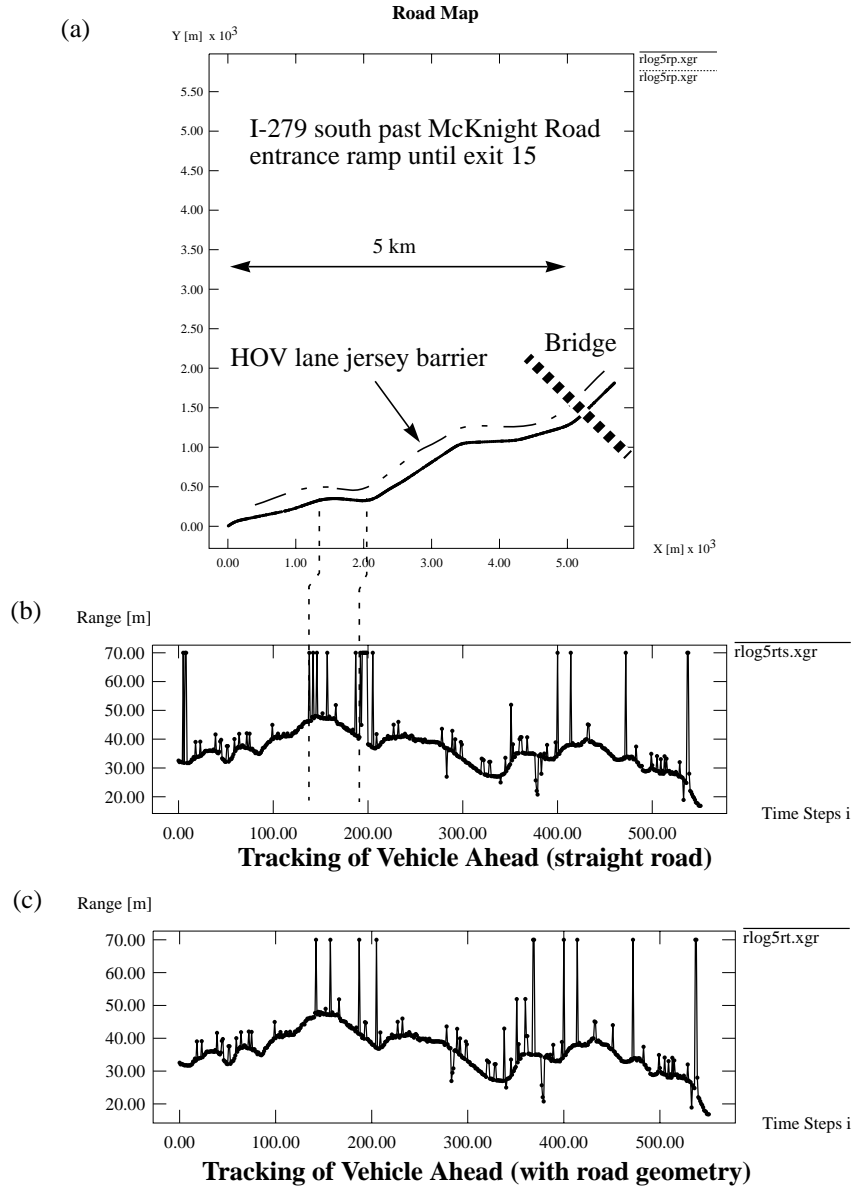


Figure 4.9 Tracking vehicle ahead in driving lane (Radar & Vision)

Results using Vision

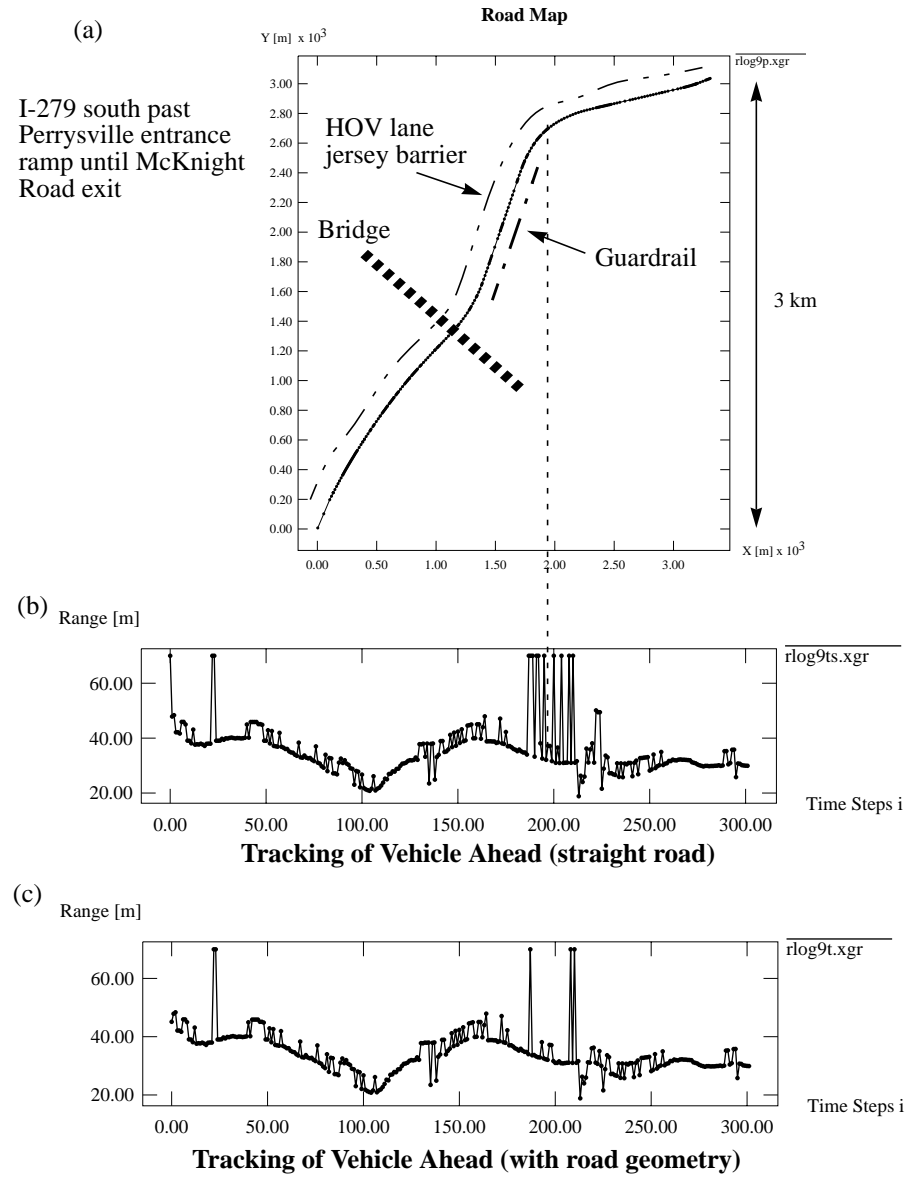


Figure 4.10 Tracking vehicle ahead in driving lane (Radar & Vision)

In addition, for this integrated system, we implemented a procedure to eliminate ghost targets (see CHAPTER 3, section 3.5). Due to RALPH's image processing procedures and evaluations, we can be fairly certain that no obstacles are present in RALPH's immediate field of view. Using a flat earth geometry projection and camera calibration to compute range, we can eliminate ghost targets that are mirror imaged into the driving lane within RALPH's field of view.

However, it would be advantageous to be able to sense road geometry over a range that matches that of the radar sensor. Therefore, in the following section, we will describe another approach to the problem, using a GPS / digital road-map based system instead of RALPH.

4.4 Results using Map and GPS

Since the mid-1980s, a new satellite navigation system (GPS) has become available worldwide. Originally intended for predominantly military applications, it has become increasingly available for civilian uses in recent years. Moreover, the cost of GPS receivers has decreased dramatically and advances have been made in improving positioning accuracies. We will first give an overview of basic GPS operation and then describe how it is used in conjunction with digital road-maps in order to determine road geometry at the current vehicle location.

4.4.1 GPS Basic Operation

A fair amount of literature is available on the operation of the GPS (*Global Positioning System*), such as [13], so we will only give a brief overview in this section.

GPS consists of 24 satellites circling the earth in low orbits. At any given time, at least six satellites are almost always visible above the horizon at most points on earth. The satellites continuously transmit coded signals that can be tracked and decoded by a *receiver*. Basically, the *receiver* calculates the position of each satellite, using orbital information (ephemeris data). The distance to the satellites is computed by measuring the time of flight of a coded signal. In addition, the time stamp (clock) between tracked satellites and the *receiver* must be synchronized (see [13]). Thus, if at least four satellites are visible, the location and velocity of the *receiver* can be calculated by triangulation. Each satellite transmits two pseudo random noise (PN) code modulated signals on two different carriers in L-band. Each code has a different

Results using Map and GPS

repetition rate. Hence, the theoretical range resolution for determining satellite position depends on the type of signal used. Table 4.3 shows a summary of available signals.

Signal	Frequency [MHz]	Wavelength [m]
L1 carrier	1575.42	0.20
L2 carrier	1227.60	0.24
C/A code	1	300
P code	10	30

Table 4.3 GPS Signals

Only the C/A code signal is available to all users. However, it is intentionally degraded by a process called selective availability (SA), so that only ‘authorized’ users can obtain full accuracies. P-code signals are encrypted and available exclusively to ‘authorized’ users. C/A code is transmitted only on L1; P-code on L1 and L2.

Several sources of error influence the precision with which a *receiver* can locate its position. These fall generally into four categories:

- ***Satellite clock and ephemeris errors.***

These are due to drift in clock and uncertainty in satellite position. They could accumulate up to a 4.3 m error between updates from the GPS master ground control station.

- ***Ionospheric and tropospheric errors***

Radio signals travel at different speeds through different layers of the atmosphere. This leads to a refraction effect on the signal path, which becomes especially noticeable at low tracking elevations ($< 20^\circ$). The error can be corrected with the help of mathematical models up to a residual error of a few meters.

- ***Multipath effects***

These errors occur when the signal bounces off another surface (buildings, earth’s surface, etc.) before arriving at the *receiver* antenna. This distorts both modulation and phase. Again these errors are more prevalent at low tracking elevations ($< 20^\circ$).

Integration with Road Geometry System

- **Selective Availability (SA)**

This is a satellite clock dither error intentionally introduced by the US Department of Defense. Typically, SA location errors are 40-60 meters and can range as high as 100 meters.

One disadvantage of GPS is that it requires line of sight to the satellites in order to make a measurement. This can lead to problems in cities, tunnels, etc. However, it is possible to get around that problem by installing ground-based transmitters (or pseudolites) which broadcast signals identical to or approximating GPS satellite signals.

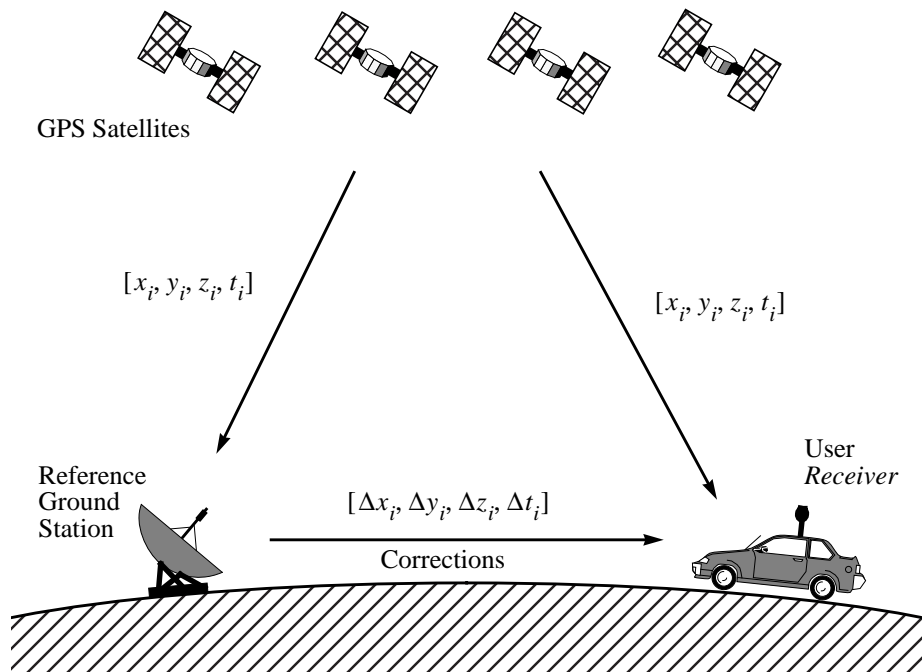


Figure 4.11 Differential GPS

Standard GPS can only give a position estimate accurate to within about 100 meters, due to the inherent errors discussed above. This is not sufficient for use in a map-based road geometry sensor. However, two additional techniques can significantly improve the position accuracy of a vehicle:

Results using Map and GPS

In **Differential GPS**, a ground base station is employed, whose correct coordinates are known. Therefore, it can compute the instantaneous error present in the GPS signal and broadcast this error to other *receivers* in the vicinity via a radio link. Differential GPS can substantially reduce all of the errors discussed above, except multipath effects. Useful differential corrections can be obtained over distances as large as 1,000 kilometers, provided the time for transmitting and processing corrections can be kept small. Figure 4.11 shows the basic setup.

In **Carrier Phase GPS**, the *receiver* tracks the phase of the carrier frequency instead of using code measurements to determine range to the satellites. A phase shift in the carrier frequency is directly proportional to a change in range and, therefore, position of the *receiver*. Phase ambiguity problems are resolved by special techniques. In addition, a continuous lock on the carriers must be maintained at all times. If the *receiver* loses phase lock, it must be reinitialized. Potentially, accuracies in the centimeter range are possible.

Table 4.4 shows the position accuracies that can be obtained with GPS, in different modes of operation. For carrier phase GPS, the number given was obtained with a unit from NOVATEL, which we were using in our experiments. Figure 4.12 shows corresponding graphs of the measured change in x-y position of a stationary *receiver* over a time period of approximately 20 minutes.

Operation Mode	Accuracy	Range	Technique used
Standard (absolute)	120 m	global	
Differential	2 - 6 m	20 km	remove position independent & time dependent bias
Carrier Phase	20 cm (Novatel)	10 km	bypass codes, use phase shift instead

Table 4.4 GPS Position Accuracies

Integration with Road Geometry System

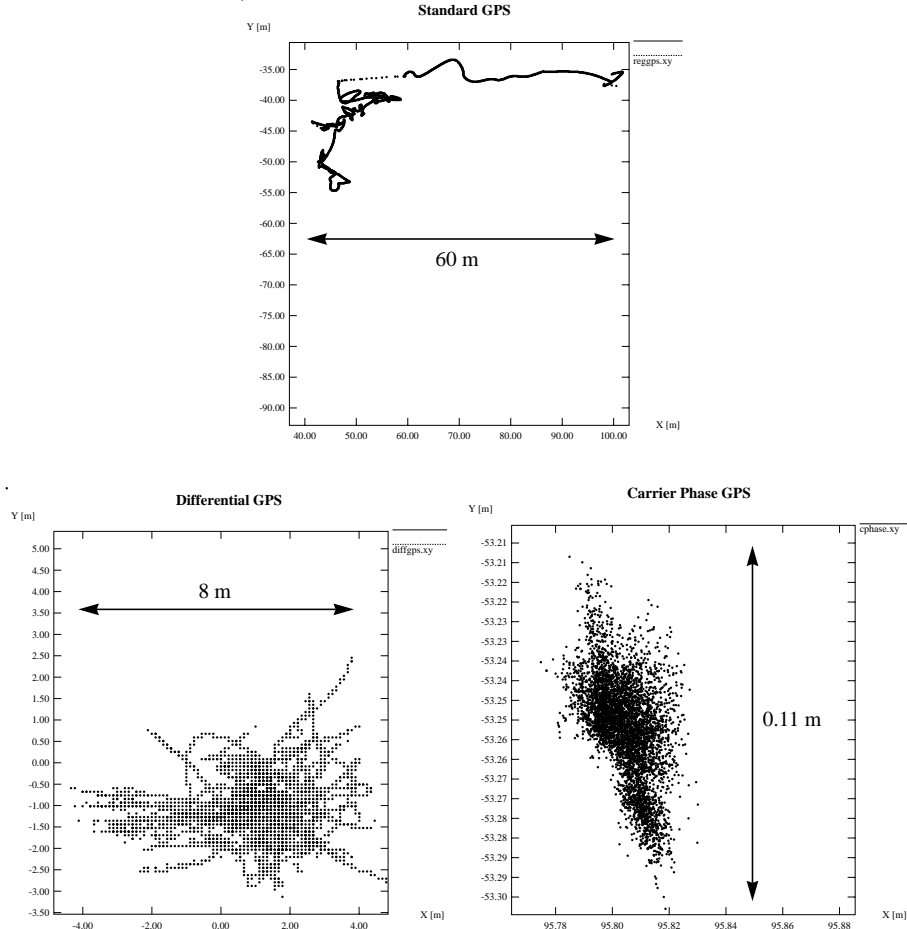


Figure 4.12 GPS position error over time for stationary *receiver*

4.4.2 Digital Road-Maps

With the advance of technology in recent years, digital maps of many urban and non-urban areas have become available. A typical map of this kind is shown in Figure 4.13 (Etak, Inc.) . Currently, the best available resolution is approximately

Results using Map and GPS

12 meters. Different types of roads are shown. Each road is split into segments, represented by a small number of position data points. With the given map resolution, individual lanes on a particular road cannot be distinguished, but it is possible to look ahead and detect approaching curves and their corresponding curvature. Also, information on road structure, such as the number of lanes, lane widths, whether it is a divided highway, etc., can easily be added.

The map resolution proved to be sufficient for determining whether objects detected by the radar sensor are located on-road or off-road.

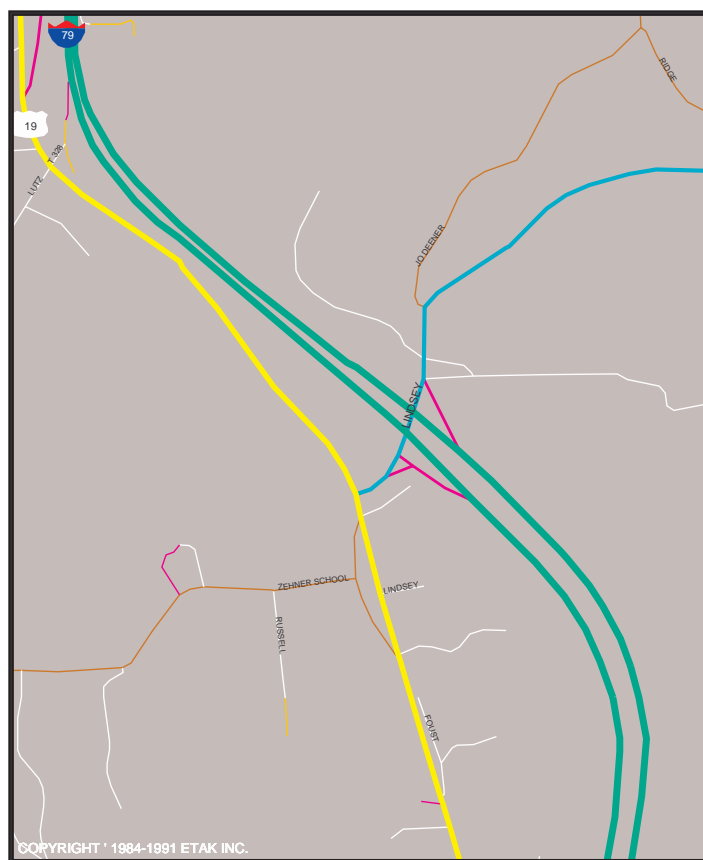


Figure 4.13 Digital Map of Urban Area (in Pittsburgh)

However, an accurate lane placement on multilane roads was not possible. As discussed in section 4.4.1, carrier phase GPS is capable of locating vehicle position with an accuracy comparable to RALPH (section 4.3). Hence, we built our own digital road-map by driving the vehicle on certain test stretches and recording vehicle position at intervals of approximately eight meters, using GPS.

4.4.3 Integrated Obstacle and Road-Map

Similar to the vision system, as described in section 4.3 , the GPS/road-map system is integrated with the radar data. The look-ahead distance of this road geometry sensing system is not limited by current environmental conditions, and it is therefore set by the user to a distance of 200 meters in order to match the maximum range of the radar sensor. Hence, no road extrapolation is necessary. The target tracking window and road lane classification method used are identical to those described in section 4.3 . As before, both the radar sensor and the GPS/road-map are calibrated with respect to vehicle origin. Hence, road points and object points are given in vehicle-centered coordinates and are thus merged. Radar data updates are still provided at 3 Hz. However, differential GPS updates are available only at 1 Hz and carrier phase GPS updates at 5 Hz. Therefore, with differential GPS we could observe some matching errors, due to time delays between both sensors which could not be completely compensated, and due to the inherent lower accuracy of differential GPS (see Figure 4.15). Unlike RALPH, the look-ahead distance for this road geometry sensor is much larger. Hence, small yaw errors in the estimation of current vehicle orientation on the road-map lead to larger road-location errors at long ranges. Especially when the vehicle is moving in a tight curve, vehicle yaw changes rapidly and time delays in the GPS position updates can lead to a significant error. Thus, in Figure 4.15 , we can observe that the tracked preceding vehicle in the driving lane is lost during the tighter curves.

Carrier phase GPS provides a faster update rate of 5 Hz and higher position accuracy that remedies some of the above problems. Similar to the results obtained in section 4.3, the combined error of carrier phase GPS for sensing road geometry, and radar for sensing object location, is small enough to reliably determine the road lane location of an object. A problem remains if the GPS loses carrier phase lock because of sudden changes in vehicle position or obstruction of line of sight to the satellites. However, these position jumps can be smoothed by integrating an IRU (**Inertial Reference Unit**) into the system. An IRU computes vehicle orientation and position information from gyroscopes and optical encoders on the wheels [13]. It is accurate over short distances (a few hundred meters on road), but suffers from cumulative errors over distance and time travelled due to wheel slip and gyroscope drifts. Nevertheless, it can augment a GPS system and correct errors over short intervals.

Results using Map and GPS

Figure 4.14 displays two snapshots of an integrated obstacle and road-map using radar and carrier phase GPS.

Figure 4.16 shows distance to a preceding vehicle tracked in the test vehicle's driving lane over time. Figure 4.16 (c) shows the result obtained when using the road geometry information given by carrier phase GPS and road-map. Figure 4.16 (a) shows the corresponding vehicle path. Figure 4.16 (b) shows the result with the same radar data, but without the use of road geometry data, i.e. the road lane is assumed to be always straight.

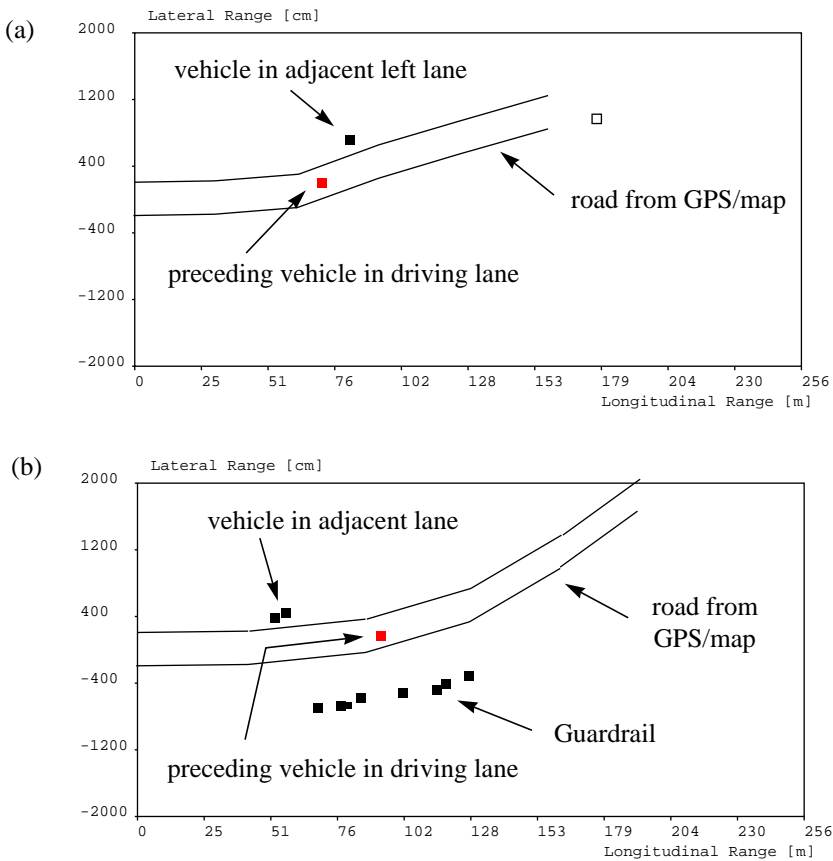


Figure 4.14 Integrated radar obstacle and GPS/road-map

Integration with Road Geometry System

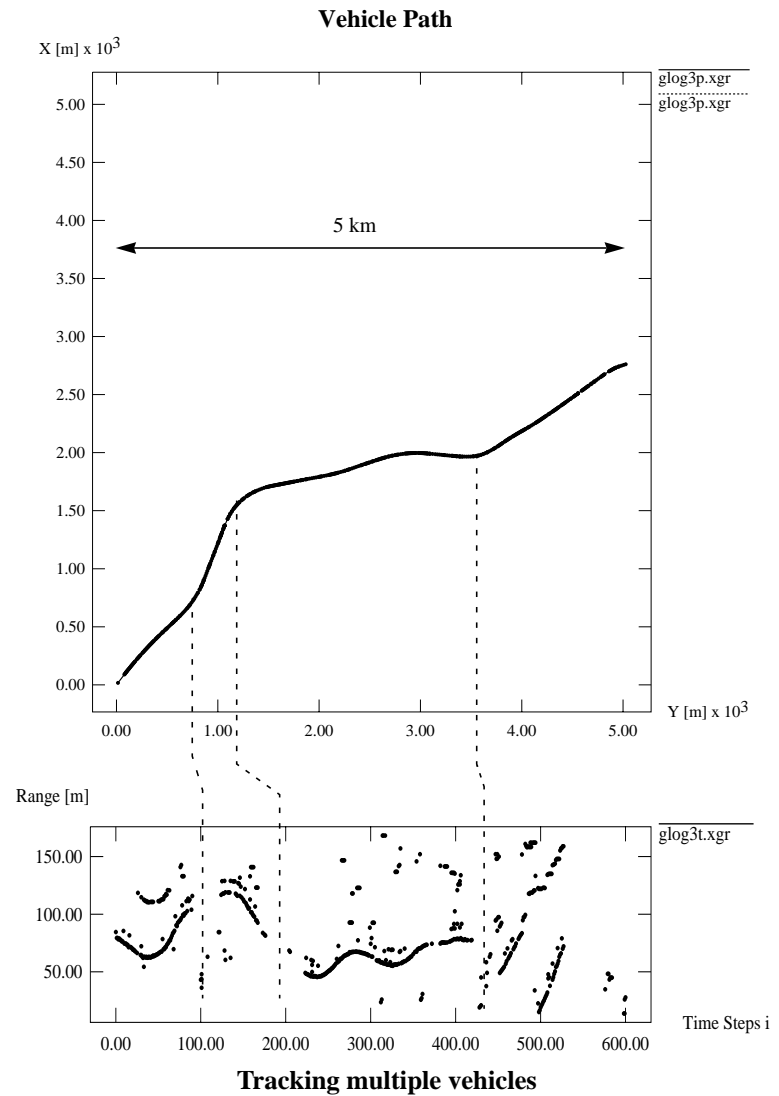


Figure 4.15 Tracking vehicles in driving lane (differential GPS)

Results using Map and GPS

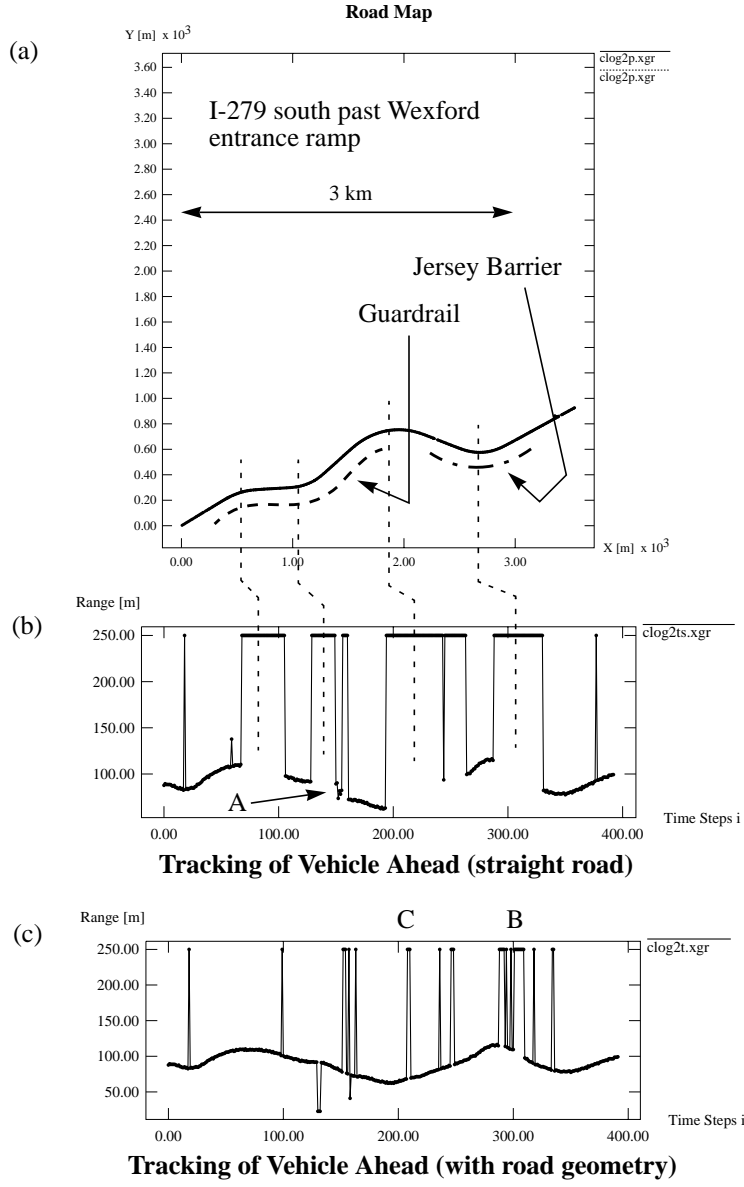


Figure 4.16 Tracking vehicle ahead in driving lane (w. carrier phase GPS)

Integration with Road Geometry System

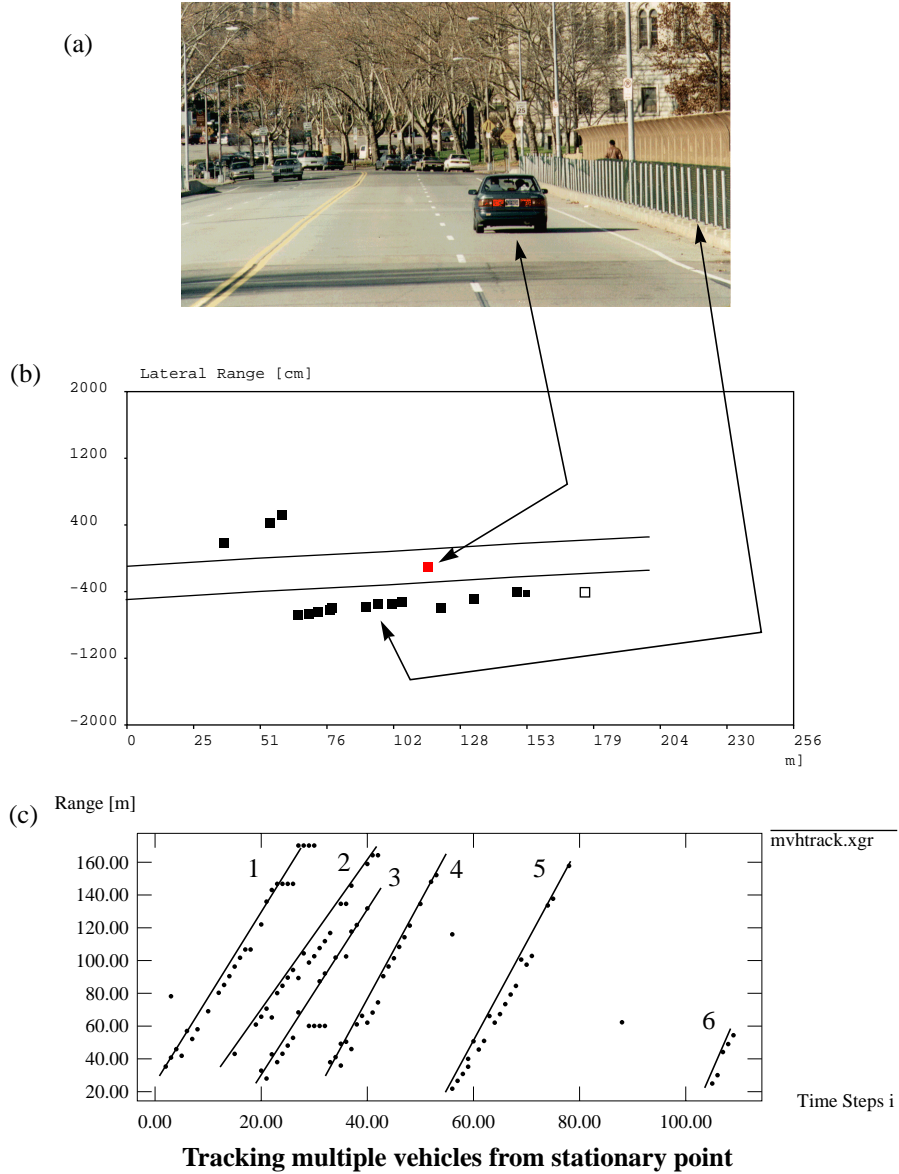


Figure 4.17 Tracking vehicles in cluttered environment

Results using Map and GPS

We can also make several additional observations, marked by A, B and C in Figure 4.16 : ‘A’ denotes a point where we erroneously detect the guardrail in our driving lane, as in this particular sequence we assumed a straight road. In ‘B’, the car being tracked, momentarily went outside the field of view of the radar because of the road curvature. Point ‘C’ is an outlier in GPS data, where current vehicle heading was computed incorrectly.

Again we can observe in general, as indicated in the figure, that the performance of the integrated system is much better on curved road segments.

Figure 4.17 shows results obtained when tracking multiple vehicles over time in a cluttered environment from a stationary point. A snapshot of the traffic scene is displayed in Figure 4.17 (a) and (b). Our vehicle, carrying the radar, was parked in a safe spot overlooking the left lane in the direction of traffic. The tracking road window was placed in the right lane, next to the guard fences, as displayed in Figure 4.17 (b). In Figure 4.17 (c), we can observe the traces of multiple vehicles over time as they drive past in the right lane. Each string of diagonal points represents an individual vehicle. Traces 2 and 3 appear a little noisier. However, this can be explained by the fact that these vehicles were driving fairly close together and the second vehicle (trace 3) was sometimes shadowed by the first (trace 2).

Integration with Road Geometry System

Genius is one percent inspiration and ninety-nine percent perspiration.

----- Thomas Edison

The goal of this thesis research was to develop a sensing system capable of providing relevant information about the local traffic situation to an intelligent cruise control (ICC) or a human driver. The core of the system is an integrated radar sensor linked to a road geometry sensor and database. We use road geometry information for radar target classification and clutter rejection. As an improvement over current systems, it is able to operate on a highway, as well as in more cluttered environments, such as rural and city roads. Currently, rural road accidents cause the largest number of fatalities, and the largest total number of accidents occurs in city traffic.

The radar sensor design operates at a carrier frequency of 76.5 GHz, which was recently approved by the FCC for automotive radar applications within a 1 GHz bandwidth. The radar uses a single transmitter and four identical receiver channels. The transmitted waveform is frequency modulated giving target range. Target bearing information is available through wavefront reconstruction techniques. The radar sensor thus demonstrates the ability to achieve high resolution target location detection with a minimal amount of hardware and no mechanical scanning mechanism. Choosing a millimeter wave radar as range sensor over a laser- or vision-based range sensor also proved its perception ability to operate more robustly under different weather and other environmental conditions.

Conclusions

Most other existing sensor design prototypes are restricted in their field of view and resolution, because they use a limited number of discrete multiple beams.

Two different methods for sensing road geometry were integrated with the radar sensor. The first method is vision-based, and the second one uses GPS vehicle position information in conjunction with a road-map database. In terms of accuracy of detecting road location, both methods showed similar performance results.

The vision approach has the advantage that no preliminary information about the road is needed. The system rapidly adapts to any existing road. However, its maximum look-ahead distance is limited to a range shorter than the maximum detection range of the radar sensor. Also, being a vision sensor, it depends upon available lighting conditions and thus performs less well in inclement weather (fog, rain, snow) and darkness.

The GPS / road-map based sensing system, on the other hand, has the advantage of being able to match its look-ahead distance to the maximum detection range of the radar. Also, it is weather independent because it uses radio signals. But GPS requires line of sight to the satellites in order to operate properly. Hence, it is not as reliable in urban areas, tunnels or mountainous regions. However, some of these problems can be remedied by the use of ground repeater stations. In addition, this road geometry sensing system needs a preliminary road-map database in order to be able to operate. Generally speaking, this is a disadvantage because it limits the area of operation of the system. But, in the near future, road-map databases for most parts of a country in North America, Japan or Europe, will become available, because these are also used for traveller navigation aids which will become a more common feature in many automobiles.

5.1 Contributions

The main contributions of this thesis research are as follows:

- Design and development of the first non mechanically scanned FMCW millimeter wave radar sensor for automotive applications, using wavefront reconstruction techniques to obtain target bearing.
- Integration of radar and road geometry sensor for classifying roadway obstacles with respect to the own vehicle's driving lane, resulting in a considerably improved clutter rejection.

Directions for Future Work

This work demonstrates the first successful integration of a road geometry sensing system with an improved high resolution, electronically scanned radar sensor, to achieve a better and more robust driving system for autonomous vehicles and / or electronic driver assistance.

5.2 Directions for Future Work

A variety of improvements are possible for the present system, some of which could remedy inadequacies discussed in previous chapters.

One of these would be changes to the current antenna design in order to avoid ghost targets in bearing. This would consist most likely of a new hardware design. Generally speaking, it is possible to improve the antenna sidelobe suppression level from the current -9 dB to about -20 dB.

An alternative or additional approach may be a combination of hardware and software. As discussed in section 3.5, the path difference between the two outermost receivers of the antenna to a target is too small in order to detect it reliably and decide on which side the target is located. However, an additional receiver could be located at an arbitrary different location, thereby increasing the available baseline between the outermost receivers. This would increase the path difference and put it in a range that makes it detectable by software. In this way, any mirror-imaged ghost targets could be eliminated.

It was shown that the available resolutions in range and bearing are sufficient for most traffic situations. But in certain circumstances a higher resolution ability in bearing may be desired. This could be achieved in hardware by doubling the number of receiver channels to eight, which would increase the available resolution from 3° to 1.5° . The same effect can also be achieved with less hardware effort by employing a second transmitter antenna at a different location and switching between both antenna location. This effectively also increases the number of data points in the spatial domain to eight and thus increases angular resolution correspondingly. A brief description of the method is given in [1].

Alternatively, the resolution abilities of the radar system in both range and bearing could be improved by applying high resolution spectral estimation techniques (refer to [12]). Most of these methods are unfortunately computationally quite expensive and it would be necessary to derive an approach, possibly in conjunction with a DSP processor, that would make a real-time application feasible (refer also to [3]).

Conclusions

On the radar sensor system one could switch the modulation from a simple triangular waveform to a coded FM waveform. This would make the sensor operation more robust in an environment where a large number of similar sensors are employed. The current modulation scheme is already quite robust against interference from other sensors, partly because sweep duration is short compared to sweep repetition rate. However, considerable improvements could be made by moving to a coded modulation waveform.

In addition, polarization filters could be used in front of the antenna. If wave polarization is rotated by 180° between transmitter and receiver, then all transmission from a different transmitter into the receivers is blocked. Also, each reflection from an object rotates the wave polarization by approximately 180° . Hence, all even multipath reflections can be suppressed which would reduce overall clutter and errors due to ground returns.

The current radar front end has been built in standard waveguide technology. The hardware is reliable and robust, but it also requires a fairly large amount of space. It would therefore be advantageous to move future designs to hybrid or MMIC technology and thus miniaturize the front end. Unfortunately, MMICs are not yet readily available at 77 GHz. As the required investments tend to be quite high, this can probably be done only as part of an industrial project.

However, through the PROMETHEUS project in Europe and the current AHS project in the USA, there is a strong interest in automotive radars and thus at the moment a corresponding technology development. It is therefore quite likely that within a few years low cost millimeter radar components are available.

Appendix A

Money won't buy happiness, but it will pay the salaries of a large research staff to study the problem.

----- Bill Vaughan

A.1 Derivation of Range Accuracy

Quite often we use the logarithmic unit [dB] to describe the ratio of output to input signal amplitude, or to express a Signal-to-Noise Ratio (SNR):

$$P_{[dB]} = 20\log \frac{s_{out}(t)}{s_{in}(t)} \quad (\text{A.1})$$

Generally a signal can be described as a signal voltage level $S(t)$ or a signal power level $P(t)$. Signal power is proportional to the square of signal voltage ($P = V^2/R$). A conversion to [dB] always expresses a power ratio. Hence, we use either one of the relationships given below to compute, for example, the SNR in [dB], depending on whether the inputs are signal voltages $S(t)$ or signal powers $P(t)$:

$$\text{SNR: } P_{\text{SNR [dB]}} = 10\log P(t) = 20\log S(t)$$

Appendix A

The theoretical SNR of an A/D converter can be calculated by the following formula:

$$\text{Max. SNR} = \frac{(\text{FSR}/\sqrt{2})}{(0.5 \cdot \text{LSB}/\sqrt{3})} = \frac{\pm 2048/\sqrt{2}}{0.5/\sqrt{3}} = 74 \text{ [dB]} \quad (\text{A.2})$$

where FSR is the Full Scale Range. The result given is for a 12-bit ADC in bipolar mode. However, in general, a better approximation in practice is given by the rule of thumb of calculating SNR as 6 dB per bit of ADC resolution, subtracting 6 dB for the bipolar case.

Typically, however, for a real target the Signal-to-Noise Ratio is much smaller. A 12-bit ADC has a total of 4096 increments. The noise amplitude that we observed when putting an absorber in front of the radar antenna is about 5 increments, after removing systematic errors.

The signal amplitude for a 7 m^2 target is approximately 160 increments at a range of about 80 meters as measured in experiments described in CHAPTER 3, section 3.4.1. In this case, therefore the Signal-to-Noise Ratio is approximately $160/5 = 32 \approx 30 \text{ dB}$.

For a signal: $S(t) = A \sin \omega t$

the rms value is $= A/\sqrt{2}$
and rms power is $= A^2/2 = 10\log(A^2/2) \text{ [dB]}$

In [26] it is shown that generally the rms error δM of a radar measurement M can be expressed as

$$\delta M = \frac{kM}{\sqrt{2 \text{ SNR}}} \quad (\text{A.3})$$

where k is a constant and SNR is the signal to noise ratio (in linear units).

Based on the rms range error expressions for a two frequency CW system, we will now derive the respective error expression for a FMCW system. In [26] the equations for calculating target range and rms range error for a two frequency CW system are given by

Miscellaneous Units

$$R = \frac{c}{4\pi \Delta f_{12}} \cdot \Delta\phi \quad \delta R = \frac{c}{4\pi \Delta f_{12} \sqrt{2 \text{ SNR}}} \quad (\text{A.4})$$

where Δf_{12} is the difference between the two frequencies and $\Delta\phi$ the respective phase difference to the target.

Rewriting equation (2.1) in CHAPTER 2 we have the calculation of range for a FMCW radar system (sawtooth modulation)

$$R = \frac{c}{4\Delta f} \cdot \frac{\tilde{f}_b}{\tilde{f}_m} \quad (\text{A.5})$$

Comparing equations (A.4) and (A.5), the theoretical rms range error for a FMCW system can then be expressed as

$$\delta R = \frac{c}{4\Delta f \sqrt{2 \text{ SNR}}} \quad (\text{A.6})$$

A.2 Miscellaneous Units

In the area of radio frequency electronics, three other units which are commonly used are [dB_i], [dB_c] and [dB_m]:

[dB_i] is used to describe the gain of a directional antenna with respect to an isotropic antenna. An isotropic antenna radiates energy equally in all directions.

[dB_c] describes the power ratio between carrier wave and harmonic wave in a signal.

[dB_m] is quite often used to describe low signal power in transmitter or receiver electronics rather than using milliwatts [mW]. The conversion between [dB_m] and [mW] is given as follows:

$$P_{[\text{dBm}]} = 10 \log P_{[\text{mW}]} \quad \text{and} \quad P_{[\text{mW}]} = 10^{P_{[\text{dBm}]} / 10} \quad (\text{A.7})$$

Appendix A

Hence,

$$\begin{aligned} 0 \text{ [dBm]} &\equiv 1 \text{ [mW]} \\ -30 \text{ [dBm]} &\equiv 1 \text{ [\mu W]} \end{aligned} \tag{A.8}$$

Note:

$$\begin{aligned} 0 \text{ dB} &\equiv \text{ratio of } 1 \text{ mW} \\ 0 \text{ dBm} &\equiv \text{absolute value of } 1 \text{ mW} \end{aligned} \tag{A.9}$$

Appendix B

Never make anything simple and efficient when a way can be found to make it complex and wonderful.

B.1 Hardware and Software Implementation Issues

Figure 2.4 in CHAPTER 2 shows a block diagram of the radar hardware. Most of the millimeter wave front-end components are standard parts that can be obtained from a catalogue. Only the power divider and the antenna assembly are custom designed in order to obtain an array radar receiver. The maximum IF was chosen to be 500 kHz. The analog signal is then digitized with 12 bit at a sampling rate of 2.5 MHz, and data from all four channels is stored sequentially in a FIFO. Digitization and data transfer logic are controlled by GAL (*Gata Array Logic*) ICs and a Motorola 68HC11 microcontroller. The microcontroller also facilitates communication to the outside world, i.e. a user's host computer, via a RS-232 serial line. Unfortunately this serial line cannot run faster than 9600 baud on an HC11. However, it is fairly straightforward to upgrade this link to a higher speed parallel line. In addition, the HC11 microcontroller oversees the transfer of raw radar data to the C40 DSP and controls the transfer of processed radar data from the C40 via the HC11 to the host computer (see Figure B.1).

Appendix B

The user can select from up to four different FM modulation waveforms which are stored in EEPROM. A single FM sweep and data acquisition is started by sending a trigger command via the serial line to the HC11. After the respective acquisition and processing delay times, radar target information on range, bearing, amplitude and, optionally, doppler velocity is returned to the user via the serial line.

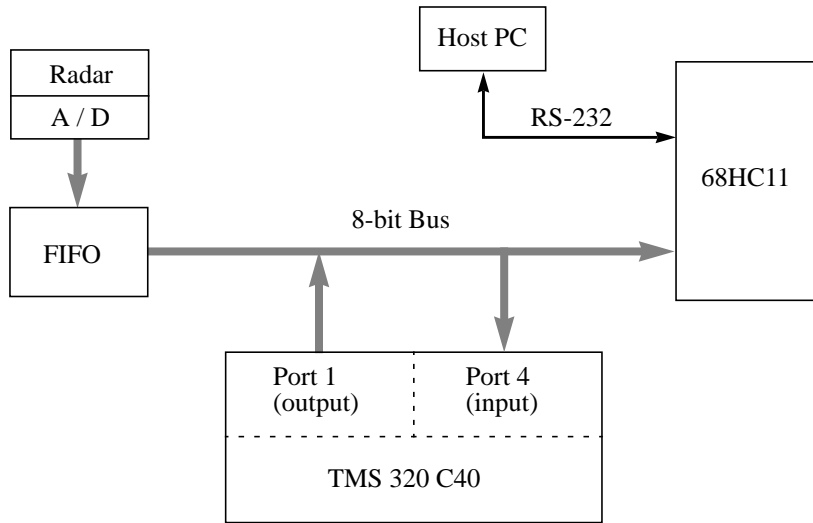


Figure B.1 Data transfer connections

As shown in Figure B.1, data is transferred from the radar FIFO to the C40 processor via C40 port 4, using DMA channel 4. C40 port 1 then outputs the processed data to the user via the HC11 microcontroller. FFT processing can be implemented efficiently on a C40 processor in assembly language, making use of the built-in bit-reversed addressing and parallel instruction set. Examples for this code are given in the User's Guide [32]. In order to obtain maximum execution speed for the FFT processing, the data is transferred from C40 global memory to the 2 Kbyte higher speed on-chip SRAM, using DMA channel 0 (see also section B.2).

It should be noted that all variable types on the C40 are represented as 4-byte words. Thus, for floating point computations we have only single precision available, and care has to be taken to ensure the numerical stability of calculations. Therefore, the formula for computing power spectral density (Psd) in decibel [dB] was modified as shown in equation (B.1) below, given real (Re) and imaginary (Im) components of a data point.

$$F = Im/Re$$

$$Psd = 20 \cdot [2 \cdot \log(Re) + \log(1 + F^2)] \quad (\text{B.1})$$

Figure B.2 shows a software flow diagram of data processing on the C40 DSP.

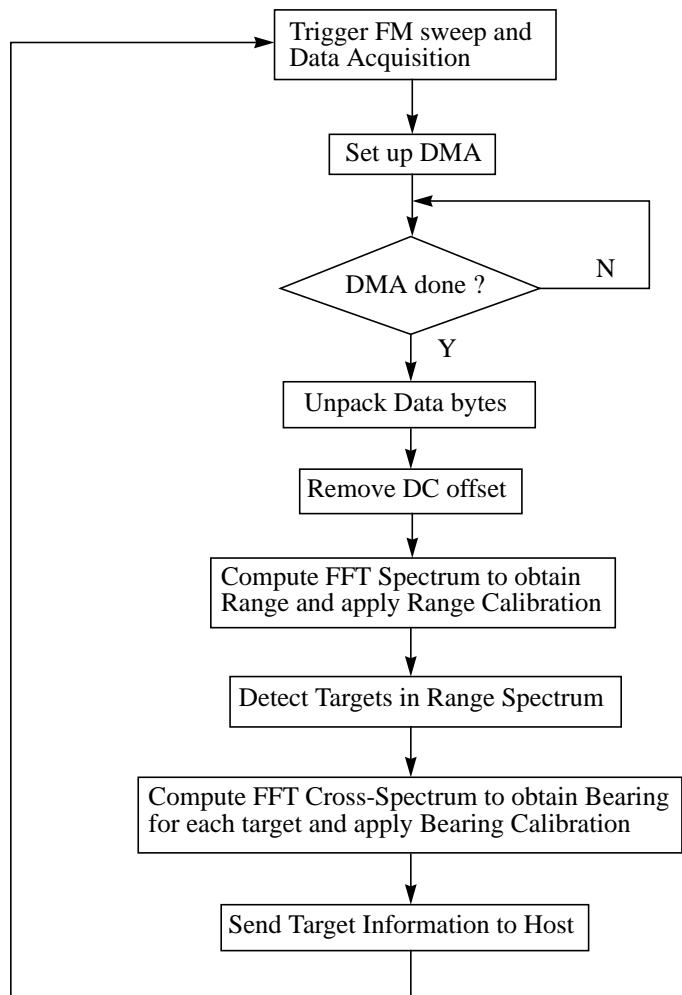


Figure B.2 C40 software flow diagram.

Appendix B

The main program as implemented on the C40 DSP is listed below. It shows program initialization on startup, DMA set up for channel 4 and the main program loop corresponding to the flow diagram in Figure B.2. A few lines of code for memory allocations and debugging were omitted for easier reading.

For further details on hardware and software implementation, refer to [15].

```
#include <intpt40.h>
#include <dma40.h>

#define NSAMP      1024
#define PACKETSIZ 4*NSAMP
#define REST       100

static volatile DMA_REG *dma_radar_in ;

volatile int *addressi, *addresso ; /* See page 2-35 of */
/* C-compiler manual */
volatile int *cpcr4 ; /* Use volatile for predefined memory */
/* locations to avoid wrong optimization */

main()
{
    static float *RawData ;
    int      *NewRdata ;

    addressi = (int *) (0x100081); /* Port 4: Input register */
    addresso = (int *) (0x100052); /* Port 1: Output register */
    cpcr4   = (int *) (0x100080); /* Port 4: Control register */

    reset_iif_flag (12); /* Set Bit 12 = 0 */
    set_iif_flag (13); /* Set Bit 13 = 1, IIOF3 is output pin*/
    reset_iif_flag (14); /* Set Bit 14 = 0, IIOF3 pin = L */
    /* i.e. CONFIG = H */

    *dma_radar_in = DMA_ADDR(4) ;

    NewRdata = (int *) malloc ((PACKETSIZ + REST)*sizeof(int));
    RawData = (float *) malloc ((NSAMP*4) * sizeof(float)) ;

    load_iie (0x22000000) ; /*enable DMA 4 and DMA 0 interrupt*/
    reset_iif_flag (DMA4_FLAG) ;
    reset_iif_flag (DMA0_FLAG) ;
```

Hardware and Software Implementation Issues

```
CACHE_ON( ) ;
while (1)
{
    dma_radar_in->dma_regs.src = (void *)0x00100081;
                                /* Port4; input */
    dma_radar_in->dma_regs.src_idx = 0;
    dma_radar_in->dma_regs.count = 0 ;/* Primary channel */
                                /* (Out), not used */
    dma_radar_in->dma_regs.dst = NewRdata;
    dma_radar_in->dma_regs.dst_idx = 1;
    dma_radar_in->gctrl._intval = 0x030A4095 ;/*Split Mode*/
                                /*Ch. 4 Read */
    dma_radar_in->dma_aux_count = PACKETSIZE ; /* Auxiliary*/
                                /* channel (In)*/
    load_die (0x00100000) ;
    reset_iif_flag(14) ;

    while (!chk_iif_flag (DMA4_FLAG)) ;

    reset_iif_flag (DMA4_FLAG) ;
    set_iif_flag(14) ;

    UnpackData (NewRdata, RawData, NSAMP) ;
    Remove_DC_offset (RawData, NSAMP) ;
    ProcessDataC40 (RawData, ...., ...., ....) ;

    SendRadarTargets (.....) ; /* via 68HC11, RS-232 */
}
} /* End of main */
```

Appendix B

B.2 Timing and Optimizations on C40 DSP

The following table shows various timings measured for program and function executions on the C40 DSP.

Function Description	Timing in [ms]
FFT written in C as given in [24] (1024 point complex)	10.68
FFT written in C40 Assembly as given in [32] using memcpy	2.3
FFT written in C40 Assembly as given in [32] using DMA 0	1.9
FFT written in C40 Assembly as given in [32] only	1.73
FFT written in C40 Assembly benchmark as given in [32]	1.56
Process all Data for 2 simulated targets, computing Window Fct.	201
Process all Data for 2 simulated targets, using Window Fct. Look-up table	77.8
Data Acquisition (FM Sweep)	~ 1.0
DMA data transfer from Radar FIFO to C40 memory	1.4
Unpack data packets received from Radar FIFO.	1.52

B.3 RCS of a Corner Cube Reflector

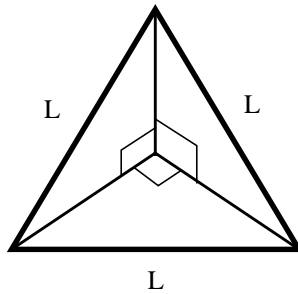


Figure B.3 Corner Cube Reflector

The general formula for calculating the Radar Cross Section (RCS) of a corner cube reflector is given by,

$$\text{RCS} = \frac{\pi \cdot L^4}{3\lambda^2} \quad (\text{B.2})$$

where λ is the center transmit wavelength and L is the length of each side.

For the experiments described in CHAPTER 3 we used corner cube reflectors with a RCS of 1.0 m^2 and 6.6 m^2 at 77 GHz.

Appendix B

Appendix C

Perception, then, emerges as that relatively primitive, partly autonomous, institutionalized, ratiomorphic subsystem of cognition which achieves prompt and richly detailed orientation habitually concerning the vitally relevant, mostly distal aspects of the environment on the basis of mutually vicarious, relatively restricted and stereotyped, insufficient evidence in uncertainty-gearred interaction and compromise, seemingly following the highest probability for smallness of error at the expense of the highest frequency of precision. ----- Egon Brunswik.

That's a simplification. Perception is standing on the sidewalk, watching all the girls go by. ----- From "The New Yorker," December 19, 1959.

C.1 Technical Specifications of Radar Sensor

Carrier Frequency	76.5 GHz
Modulation Waveform	FMCW
Swept Frequency	300 MHz
Maximum IF	500 kHz

Appendix C

Sample Rate (12 bit A/D)	2.5 MHz
Range Coverage Resolution Accuracy	1 - 200 m 1 m 0.1 m (or better)
Azimuth Coverage Resolution Nominal Accuracy	12° 3° 0.1°
Elevation Coverage	3°
Range Rate Coverage Resolution Accuracy	(Tentative Specifications) -32 to +32 m/s 0.2 m/s 3 m/s
Modulation Cycle Sawtooth Triangular Unambiguous Range	1.25 kHz 625 Hz 1200 km
Processing Time	~ 2 ms per target
Update Rate	~ 12 Hz (configurable to 70 Hz for single target)
Target Tracking	Yes
Antenna	1 Transmitter, 4 Receiver linear array VFoV: 3° , HFoV: 12° for each Antenna
Scanning Mechanism	Wavefront reconstruction by spectral analyses. Angular resolution cell: 3° x 3°
Primary Power	~ 100 W
Transmit Power	30 mW
Data Interface	RS-232 and optionally 8 bit parallel

Bibliography

-
- [1] M. Bockmair. *Mikrowellenabbildung im Nahbereich*. Phd Dissertation, Technische Universität München, 1989.
 - [2] P. Cao, J. Cuschieri and R. Sudhakar. A High Resolution 3-D Sonar Imaging System For Autonomous Underwater Vehicles. In *Proc. of Oceans '91*. Honolulu, HI. October 1991.
 - [3] P. Cao. *Digital Signal Processing for a High-Resolution Three-Dimensional Sonar Imaging System for Autonomous Underwater Vehicles*. Florida Atlantic University, 1992.
 - [4] R. Colgin. *Description and Analysis of a Bayesian CFAR Processor in a Nonhomogenous Clutter Background*. Phd Dissertation, Oakland University, Rochester, Michigan, 1995.
 - [5] N. Currie, C. Brown. *Principles and Applications of Millimeter-Wave Radar*. Artech House, 1987.
 - [6] Jerry Eaves and Edward Reedy. *Principles of Modern Radar*. Van Nostrand Reinhold Company, 1987.
 - [7] *Encyclopaedia Britannica*. Macropaedia, Vol. 15, 1974. Keyword *Radar*.
 - [8] Frederic Harris. On the Use of Windows for Harmonic Analysis with the Discrete Fourier Transform. *Proceedings of the IEEE*, Vol. 66, No.1, January 1978
 - [9] Martial Hebert, Charles Thorpe, Anthony Stentz. *Intelligent Unmanned Ground Vehicles*. Kluwer Academic Publishers, 1997.

-
-
- [10] T. Jochem, D. Pomerleau, B. Kumar, J. Armstrong. PANS: A Portable Navigation Platform. *Proceedings of IEEE Intelligent Vehicles Symposium*, Detroit, MI, September 1995.
- [11] S. Kay. *Modern Spectral Estimation*. Prentice Hall, Englewood Cliffs, 1988.
- [12] S. Kay and L. Marple. Spectrum Analysis - A Modern Perspective. *Proceedings of the IEEE*, Vol. 69, No. 11, November 1981.
- [13] Alonso Kelly. *Modern Inertial and Satellite Navigation Systems*. Technical Report, Carnegie Mellon University, The Robotics Institute, 1994, CMU-RI-TR-94-15.
- [14] Karl Kluge and Charles Thorpe. Explicit Models for Robot Road Following. *Vision and Navigation: The Carnegie Mellon Navlab*. Kluwer Academic Publishers, 1990, Chapter 3.
- [15] D. Langer. *Design of a 77-GHz FMCW Radar System*. Technical Report, Carnegie Mellon University, The Robotics Institute, 1997, CMU-RI-TR-97-04.
- [16] D. Langer, J. K. Rosenblatt and M. Hebert. A Reactive System For Off-Road Navigation. In *Proc. IEEE Conference on Robotics and Automation*, 1994.
- [17] D. Langer and C. Thorpe. Sonar based Outdoor Vehicle Navigation and Collision Avoidance. *Proceedings IROS' 92*. Raleigh NC.
- [18] D. Langer, C. Thorpe. Range Sensor Based Outdoor Vehicle Navigation, Collision Avoidance and Parallel Parking. In *Autonomous Robots*, Vol.2, No.2, August 1995.
- [19] Albrecht Ludloff. *Handbuch Radar und Radarsignalverarbeitung*. Vieweg Verlag, 1993, sections 2.5 and 9.
- [20] Lawrence Marple. *Digital Spectral Analysis with Applications*. Prentice Hall, Englewood Cliffs, 1987.
- [21] A. Oppenheim and R. Schafer. *Discrete-Time Signal Processing*. Prentice Hall, 1989.
- [22] D. Pomerleau. *Neural Network Perception For Mobile Robot Guidance*. Kluwer Academic Publishers, 1993.
- [23] D. Pomerleau, T. Jochem. Rapidly Adapting Machine Vision for Automated Vehicle Steering. In *IEEE Expert: Special Issue on Intelligent System and their Applications*, pp. 19-27, April 1996.
- [24] W. Press, B. Flannery, S. Teukolsky, W. Vetterling. *Numerical Recipes in C*. Cambridge University Press, 1988. Chapter 12.
- [25] M. Rozmann, M. Lange, J. Detlefsen. Collision Avoidance Radar Using Wavefront Reconstruction. In *Proc. 3rd PROCHIP Workshop*, Paris, May, 14th 1990, pp 251-256.
- [26] M. I. Skolnik. *Introduction to Radar Systems*. McGraw-Hill, 1980, 2nd edition, pages 87, 96-97, 401.

-
-
- [27] Samuel Stearns and Ruth David. *Signal Processing Algorithms*. Prentice Hall, Englewood Cliffs, 1988.
 - [28] B. D. Steinberg. *Principles of Aperture and Array System Design*. John Wiley & Sons, New York, 1976, pages 194-196.
 - [29] M. Szyper. New time domain window. *Electronics Letters*, 27th April 1995, Vol. 31, No. 9, page 707-708.
 - [30] Charles Thorpe, Martial Hebert, Takeo Kanade, Steven Shafer. Toward Autonomous Driving: The CMU Navlab. Part I - Perception. In *IEEE Expert*, 1991.
 - [31] Charles Thorpe. *Vision and Navigation: The Carnegie Mellon Navlab*. Kluwer Academic Publishers, 1990.
 - [32] Texas Instruments. *TMS320C4x User's Guide*. Texas Instruments, 1994.

